Binary black hole coalescence in the extreme-mass-ratio limit: Testing and improving the effective-one-body multipolar waveform

Sebastiano Bernuzzi, Alessandro Nagar, and Anıl Zenginoğlu

Phys. Rev. D **83**, 064010 — Published 8 March 2011

DOI: 10.1103/PhysRevD.83.064010

Binary black hole coalescence in the extreme-mass-ratio limit: testing and improving the effective-one-body multipolar waveform

Sebastiano Bernuzzi[1], Alessandro Nagar[2], and Anıl Zenginoğlu[3]
[1] *Theoretical Physics Institute, University of Jena, 07743 Jena, Germany*
[2] *Institut des Hautes Etudes Scientifiques, 91440 Bures-sur-Yvette, France and*
[3] *Theoretical Astrophysics, California Institute of Technology, 91125 Pasadena, CA*

We discuss the properties of the effective-one-body (EOB) multipolar gravitational waveform emitted by nonspinning black-hole binaries of masses μ and M in the extreme-mass-ratio limit, $\mu/M = \nu \ll 1$. We focus on the transition from quasicircular inspiral to plunge, merger and ringdown. We compare the EOB waveform to a Regge-Wheeler-Zerilli (RWZ) waveform computed using the hyperboloidal layer method and extracted at null infinity. Because the EOB waveform keeps track analytically of most phase differences in the early inspiral, we do not allow for any arbitrary time or phase shift between the waveforms. The dynamics of the particle, common to both wave-generation formalisms, is driven by leading-order $\mathcal{O}(\nu)$ analytically–resummed radiation reaction. The EOB and the RWZ waveforms have an initial dephasing of about 5×10^{-4} rad and maintain then a remarkably accurate phase coherence during the long inspiral (~ 33 orbits), accumulating only about -2×10^{-3} rad until the last stable orbit, *i.e.* $\Delta\phi/\phi \sim -5.95 \times 10^{-6}$. We obtain such accuracy without calibrating the analytically-resummed EOB waveform to numerical data, which indicates the aptitude of the EOB waveform for LISA-oriented studies. We then improve the behavior of the EOB waveform around merger by introducing and tuning next-to-quasi-circular corrections both in the gravitational wave amplitude and phase. For each multipole we tune only four next-to-quasi-circular parameters by requiring compatibility between EOB and RWZ waveforms at the light-ring. The resulting phase difference around merger time is as small as ± 0.015 rad, with a fractional amplitude agreement of 2.5%. This suggest that next-to-quasi-circular corrections to the phase can be a useful ingredient in comparisons between EOB and numerical relativity waveforms.

PACS numbers: 04.30.Db, 95.30.Sf,

I. INTRODUCTION

In the last few years numerical and analytical relativity have demonstrated how to use information from the strong-field-fast-motion regime of coalescing black-hole binaries to build accurate analytical models of their dynamics and of the gravitational radiation emitted [1–11]. Although numerical relativity (NR) simulations of binary black holes (BBHs) have reached a high degree of accuracy and flexibility [12–16], a comprehensive spanning of the multidimensional parameter space remains prohibitive. Analytical models are thus of fundamental importance to set up the bank of gravitational wave (GW) templates for detection. The limiting case is given by extreme-mass-ratio inspirals (EMRIs) and mergers; NR simulations simply can not access such regime and post-Newtonian (PN) techniques are inaccurate at such velocities. We need analytical models for the GW emission from EMRIs systems because they are primary target sources for LISA and because their parameter space is very large [17].

The only analytical approach currently capable of accurately following the complete dynamics and providing waveforms (inspiral-plunge-merger-ringdown) of coalescing black-hole binaries is the effective-one-body (EOB) approach to the general relativistic two-body dynamics [11, 18–22]. The EOB formalism employs *resummed* PN results (for dynamics and waveforms) in order to extend their validity in the strong-field-fast-motion regime, *i.e.* in a region where they are inaccurate in their standard Taylor-expanded form. In brief the analytical construction is based on (i) a dynamics governed by a resummed Hamiltonian and an expression for the mechanical angular momentum loss (the *radiation reaction*); and (ii) a waveform-generating algorithm which combines a prescription to resum the Taylor-expanded PN multipolar waveform up to the merger and a matching procedure to the quasi-normal-modes (QNMs) waveform to describe the post-merger phase (an oscillating black hole).

One key aspect of the EOB approach is its *flexibility* [23]. Although the formalism is based on analytical results known only at a given PN order, it is possible to take into account (yet uncalculated) higher-order effects by means of suitable *flexibility parameters*. These parameters may be determined (or just constrained) by comparison with results from numerical relativity simulations valid in the strong-field-fast-motion regime. Several recent works [2, 3, 6–8, 10] have shown how this tuning can be implemented to obtain analytical waveforms that match the numerical ones within numerical errors. The tuned EOB formalism can then be used for parametric studies.

Regge-Wheeler-Zerilli (RWZ) metric perturbation theory [24–27]. is the natural tool to compute the GW emission from a system of two nonspinning black holes, of masses μ and M, in the extreme-mass-ratio limit (EMRL) $\nu \equiv \mu/M \ll 1$. In this regime several numerical results can be used to calibrate the EOB dynamics and

waveforms [8, 28–31]. In particular, recent gravitational-self-force calculations [32, 33] helped in putting constraints on the functions entering the EOB conservative dynamics [9, 34]. Regge-Wheeler-Zerilli perturbation theory has been used for many years in the *Fourier-domain* (see for example [35] and references therein) and *neglecting radiation reaction effects*, since Davis, Ruffini and Tiomno computed the waveform emitted by a particle radially plunging into the black hole [36]. Only recently the RWZ approach has been extensively developed in the *time-domain* [37–42] with the inclusion of radiation-reaction force [32, 33, 43–45].

Time-domain simulations using perturbation theory are efficient, accurate, and complement NR simulations in EMRL. The first calculation of the complete gravitational waveform emitted during the transition from inspiral to plunge, merger and ringdown in the EMRL was performed in Ref. [43], thanks to the combination of RWZ perturbation theory and 2.5PN accurate (analytical) Padé-resummed radiation reaction force [28]. Reference [29] used that result as target waveform to assess the performances of the corresponding EOB (resummed) analytical waveform. The comparison was restricted to the quadrupole case, $m = \ell = 2$. The knowledge from that study was useful in subsequent EOB/NR waveform comparisons. The treatment of the analytical radiation reaction in the strong-field-fast-motion regime has been improved since then, thanks to a resummed and factorized form of the PN multipolar waveform [8, 29, 46].

In [45] (hereafter Paper I) two of us presented an accurate computation of the gravitational radiation generated by the coalescence of two circularized nonspinning black-holes in the EMRL. The results were obtained with an improved version of the finite-difference code of [29, 43], which implements the expression of the radiation reaction force based on the (5PN-accurate) analytical waveform resummation of [8]. The knowledge of the "exact" RWZ multipolar waveform opened the way to two main conclusions, extensively discussed in Paper I. First, the computation of the final kick velocity imparted to the system by GW emission, $v^{\rm kick}/(c\nu^2) = 0.0446$. This value proved consistent with the corresponding one extrapolated from a sample of numerical relativity simulations [47] (see Fig. 7 and Tables IV and V in Paper I), as well as with the outcome of an independent calculation that relies on a different treatment of the radiation reaction [44]. Second, it was possible to show a very good agreement (at the 10^{-3} level) between the mechanical angular momentum loss provided by the analytical expression of the radiation reaction and the GW angular momentum flux computed from the RWZ waveforms. This second result supports the consistency of our approach. Notably, the agreement between the two functions was excellent also *below* the LSO, and almost along the entire plunge phase up to merger (see Figs. 8 and 9 of Paper I). The results of [45] also turned out to be compatible with the first NR computation of BBH coalescence in the large-mass-ratio regime (1:100) [16]. Recently [48] we further improved the RWZ approach of Paper I by combining it with the hyperboloidal layer method [49]. This approach brings two main benefits. First, it allows us to extract GWs at null infinity ($\mathcal{I}^+$), thereby eliminating the gauge effects related to the GW extraction at a finite radius. In addition, because we evolve the RWZ equations on a smaller coordinate domain, we substantially improve the efficiency of our code.

The aim of this paper is to perform a detailed comparison, multipole by multipole, between the RWZ and the corresponding analytical waveforms computed within the EOB approach. For the particle dynamics both codes (RWZ and EOB) implement the resummed radiation reaction force $\mathcal{F}_\varphi$ of [8] updated to include 5PN-accurate terms also for subdominant multipoles. The latter come from the 5.5PN-accurate (Taylor-expanded) circularized multipolar waveform computed by Fujita and Iyer [46]. The particle dynamics is computed within this 5PN-accurate (resummed) approximation and is the same in both codes. For simplicity, we decided not to improve it further by tuning the resummed flux entering the radiation reaction [30, 31]. For the waveform we compare the full multipolar structure up to $m = \ell = 4$, going beyond the simple quadrupole contribution.

The waveform comparison brings new knowledge with respect to the flux comparison of Paper I (see also [29]) for two main reasons. First, we assess the performance of the resummed EOB waveform in describing the *phase* of each multipole. Second, we perform detailed analyses of the next-to-quasi-circular (NQC) corrections that are needed in the late-plunge phase. NQC effects are actually responsible for the differences in the EOB/RWZ fluxes in the strong-field-fast-motion regime, as it was pointed out in Paper I (see Fig. 8 there and also the related discussion in [29]). At the waveform level, several studies [6, 7, 10, 29] have demonstrated that NQC corrections to the EOB waveform (and radiation reaction) are needed to improve its agreement with the numerical one during the late plunge and merger phase. Previous works were restricted to the quadrupole case. Two central new benefits of this paper are (i) the assessment of the complete multipolar EOB waveform in the EMRL during the transition from inspiral to plunge and merger; and (ii) the development of a robust procedure to tune NQC corrections to the gravitational wave amplitude and *phase*.

The paper is organized as follows. In Sec. II we summarize the main features of our RWZ numerical target waveform described in detail elsewhere [45, 48]. In Sec. III we describe the structure of the multipolar EOB waveform of [8, 46], giving all the details of the implementation used here. In Sec. IV we first present our results for the inspiral phase and then describe the procedure to tune NQC parameters necessary to improve the EOB waveform at merger. The discussion is based mainly on the $\ell = 2$ multipoles. In Sec. V we assess the quality of the complete EOB multipolar waveform, discussing explicitly multipoles up to $\ell = 4$. We finally put together some

concluding remarks in Sec. VI. Two appendixes are included to complement the information given in the main text. Throughout this paper we use geometrized units with $c = G = 1$.

II. REGGE-WHEELER-ZERILLI WAVEFORMS

We compute numerical waveforms at future null infinity via the time-domain RWZ perturbative approach introduced in [43] and improved in [45, 48]. We perform a hyperboloidal evolution of the RWZ equations with a point-particle source modelling the smaller-mass black hole. The distributional δ-function representing the particle is approximated by a narrow Gaussian of finite width $\sigma \ll M$. The dynamics of the particle is started using post-circular initial data as defined in [19, 43], which generate negligible eccentricity at the beginning of the evolution. The conservative part of the dynamics is governed by the $\nu \to 0$ limit of the EOB Hamiltonian (the Hamiltonian of a particle on Schwarzschild spacetime) with the following, dimensionless variables: the relative separation $r = R/M$, the orbital phase φ, the orbital angular momentum $p_\varphi = P_\varphi/(\mu M)$, and the orbital linear momentum $p_{r_*} = P_{r_*}/\mu$, canonically conjugate to the tortoise radial coordinate separation $r_* = r + 2\ln(r/2-1)$. The expression for the analytical radiation reaction force $\hat{\mathcal{F}}_\varphi$ is described in [8, 45], and has been updated with the new terms in the resummed waveform amplitude recently computed in [46] at fractional 5PN accuracy. In the computation of $\hat{\mathcal{F}}_\varphi$ we sum over multipoles up to $\ell = 8$ included. The dynamics is then computed by solving Eqs. (1)-(7) of Paper I.

Because of the different analytical approximation to the flux and because of the hyperboloidal evolution, the RWZ waveforms employed here are *quantitatively new* with respect to those of Paper I. By contrast, at a qualitative level, there are no appreciable differences. In the following we shall comment only on the main new features of our perturbative approach. For a complete description of the method, the equations, and the notation, we refer to [43, 45, 48].

We adopt the hyperboloidal layer method for the RWZ equations to extract waves at future null infinity and to increase the efficiency of our code [49–51]. The essential ingredient of this approach is a suitable transformation of the standard Schwarzschild time coordinate t in combination with spatial compactification. We anticipate here part of the technical steps discussed in [48].

We solve the RWZ equations, written in a general coordinate system [52], using coordinates $(\tau, \rho) \in \mathbb{R}^+ \times [R_*^-, S]_{R_*^+}$. The coordinates (τ, ρ) coincide with (t, r_*) in a domain $D_{r_*}^{-+} = [R_*^-, R_*^+]$, that entirely includes the motion of the particle. The RWZ equations on $D_{r_*}^{-+}$ have then the same form as in Paper I. The spatial compactification sets in at the interface $\rho = r_* = R_*^+$ in a sufficiently differentiable way. The compactifying coordinate $\rho(r_*)$ maps the infinite r_*-domain $D_{r_*}^+ = [R_*^+, \infty)$ to the finite ρ-domain $D_\rho^+ = [R_*^+, S]$, where $S > R_*^+$ is a constant. A new time coordinate is introduced according to the prescription that the timelike Killing field is left invariant, $\partial_t = \partial_\tau$, which implies

$$\tau = t - h(r_*) \ . \tag{1}$$

The height function $h(r_*)$ is related to $\rho(r_*)$ by the condition that the representation of outgoing null rays is left invariant

$$t - r_* = \tau - \rho \ . \tag{2}$$

Equations (1) and (2) imply $h(r_*) = r_* - \rho(r_*)$ that, together with the choice of a sufficiently smooth spatial compactification, determines a (future) hyperboloidal foliation. Thus the surface $\rho = S$ corresponds to future null infinity, $\mathcal{I}^+$, and outgoing waves are evenly resolved in the compactifying coordinate ρ. Our numerical domain reads $[R_*^-, S]_{R_*^+} = [-50, 70]$ with the interface at $R_*^+ = 50$, and is covered by $N = 3001$ grid points [48].

The RWZ-based approach we use to compute the numerical target waveforms relies on certain approximations. Our first approximation is to consider the dissipative radiation reaction at leading order in the mass ratio ν, neglecting higher-order corrections that enter both the conservative and the nonconservative parts of

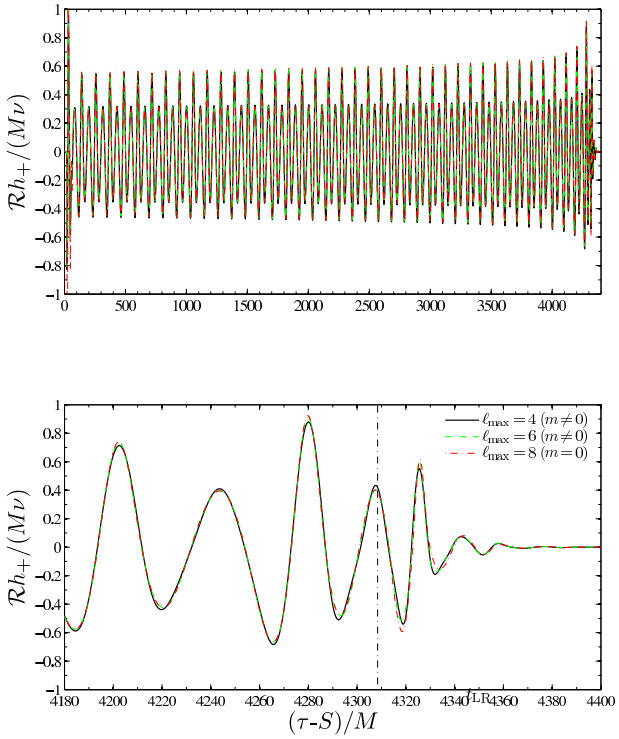

FIG. 1. Multipolar "convergence" of the $\mathcal{R}h_+/(M\nu)$ polarization of the Regge-Wheeler-Zerilli multipolar waveform. Top panel: the complete wavetrain (~ 37 cycles). Bottom panel: impact of subdominant multipoles around the merger time. The vertical dashed-line indicates the light-ring crossing.

the dynamics [32, 33, 53]. If one is interested in computing very long inspiral waveforms, these higher-order effects must be properly taken into account for LISA-related data-analysis (for example using the EOB formalism [30, 31, 45]). The computation of long inspiral waveforms with $\mathcal{O}(\nu)$ radiation reaction is affected by systematic uncertainties that depend on the mass ration, ν, and on the integration time. By constrast, when one focusses only on the late-time part of the waveform, *i.e.* the one corresponding to the "quasi-geodesic" plunge, merger, and ringdown, one can extrapolate finite-ν results to the $\nu = 0$ limit. In Paper I we followed this procedure for dynamical quantities like the kick velocity or the energy emitted during the plunge, and we showed that the impact of dealing with a finite value of ν becomes less and less important when $\nu \leq 10^{-3}$. Our second approximation is that the expression for the radiation reaction force $\hat{\mathcal{F}}_\varphi$ is based on resummed PN results for circularized binaries and, as such, it neglects non-quasi-circular corrections that explicitly depend on the radial momentum and its derivatives. The accuracy of this second approximation can be checked only a posteriori, but it is typically quite good also during the plunge [29, 45].

On the basis of the considerations of Paper I, we choose the mass ratio $\nu = 10^{-3}$ and the initial separation $r_0 = 7M$ for the present EOB/RWZ comparison. These values guarantee a long inspiral (~ 37 orbits) as well as an accurate representation of the late-time waveform (see its mild dependence on ν when moving from $\nu = 10^{-3}$ and 10^{-4} in Fig. 4 of Paper I). We follow here the same normalization convention for the RWZ $\Psi^{(\mathrm{e/o})}_{\ell m}$ master functions [with (e)ven-parity and (o)dd-parity modes] as in Paper I, *i.e.*

$$\mathcal{R}(h_+ - \mathrm{i}h_\times) = \sum_{\ell=2}^{\ell_{\max}} \sum_m \sqrt{\frac{(\ell+2)!}{(\ell-2)!}} \left(\Psi^{(\mathrm{e})}_{\ell m} + \mathrm{i}\Psi^{(\mathrm{o})}_{\ell m}\right) {}_{-2}Y_{\ell m}, \tag{3}$$

where $\mathcal{R}$ is the distance from the source, $\ell_{\max}$ is the maximum number of multipoles that we consider, and ${}_{-2}Y_{\ell m} \equiv {}_{-2}Y_{\ell m}(\Theta, \Phi)$ are the $s = -2$ spin-weighted spherical harmonics computed in the convention of Ref. [54]. Figure 1 displays various multipolar approximations to the $\mathcal{R}h_+/(M\nu)$ polarization of the RWZ waveform along the fiducial direction $(\Theta, \Phi) = (\pi/4, 0)$. The waveforms are shown versus retarded time at $\mathcal{I}^+$, $\tau - S$. The dashed line in the figure (red-online) refers to the complete waveform obtained summing the multipoles up to $\ell = 8$. The other two lines depict the partial contributions to the total waveform up to $\ell = 4$ (solid-line) or $\ell = 6$ (dash-dotted line) and neglecting the $m = 0$ multipoles. The bottom panel of the figure is a close-up on the waveform around the conventional "merger" time, *i.e.* the time t_{LR} at which the particle crosses the light-ring $r = 3M$ (vertical dash-dotted line). The figure gives us a visual idea of the impact of the various multipoles on the accuracy of the total waveform, and it indicates that $\ell_{\max} = 4$ (with only $m \neq 0$) gives us a good approximation, especially up to t_{LR}. For this reason, and to keep the discussion sufficiently simple, we shall fix $\ell_{\max} = 4$ and consider only $m \neq 0$ multipoles to compute the RWZ target waveform to be compared with the EOB analytical waveform. We will discuss the fine details of the complete RWZ waveform in [48] (see also [45]).

III. EFFECTIVE-ONE-BODY RESUMMED MULTIPOLAR WAVEFORM

In this section we review the structure of the EOB waveform [6, 8, 11, 46]. The EOB-resummed multipolar waveform can be split into two parts: the inspiral-plus-plunge-and-merger (*insplumerg*) waveform computed during the dynamics of the particle up to merger, and the *ringdown* waveform that describes the post-merger waveform as a superposition of black-hole quasi-normal modes (QNMs). A simplified and efficient representation of the transition between the late plunge and the ringdown regimes is accomplished by *matching* the insplumerg waveform to the ringdown waveform[1]. The complete EOB multipolar waveform reads

$$h^{\mathrm{EOB}\ (\epsilon)}_{\ell m}(t; a^{\ell m}_i, \sigma^{\pm}_{n\ell}) = \theta(t_m - t)\, h^{\mathrm{insplumerg}\ (\epsilon)}_{\ell m}(t; a^{\ell m}_i) + \theta(t - t_m)\, h^{\mathrm{ringdown}\ (\epsilon)}_{\ell m}(t; \sigma^{\pm}_{n\ell}) \ , \tag{4}$$

where ϵ denotes the parity, *i.e.* even ($\epsilon = 0$) for mass generated multipoles and odd ($\epsilon = 1$) for current generated ones[2]. Since the particle motion is planar, ϵ is equal to the parity of the sum $(\ell + m)$. Furthermore, we explicitly highlight the dependence on the NQC parameters $a^{\ell m}_i$ and the QNM (complex) frequencies $\sigma^{\pm}_{n\ell}$.

The ringdown waveform is written as

$$h^{\mathrm{ringdown}\ (\epsilon)}_{\ell m} = \sum_n C^{+}_{n\ell m} e^{-\sigma^{+}_{n\ell} t} + \sum_n C^{-}_{n\ell m} e^{-\sigma^{-}_{n\ell} t}, \tag{5}$$

where, following Ref. [29], we use the notation $\sigma^{\pm}_{n\ell} = \alpha_{n\ell} \pm \mathrm{i}\omega_{n\ell}$ for the positive/negative QNM frequencies and $C^{\pm}_{n\ell m}$ for the corresponding amplitudes (note that, for simplicity, we omitted here the parity index ϵ). Here $\omega_{n\ell}$ and $\alpha_{n\ell}$ indicate the frequency and the inverse damping time of each mode respectively, and $n = 0, 1, 2, \ldots N-1$ label the overtone number ($n = 0$ denoting the fundamental mode).

[1] We introduced the nomenclature "insplumerg waveform" to indicate the part of the EOB waveform that is usually called *insplunge waveform* in the literature [6, 11]. The reason for this choice is twofold. First, because it includes NQC corrections that become relevant essentially only around the merger time. Second, because it needs compatibility conditions with the RWZ waveform *around merger* to be fully determined.

[2] For notational consistency with previous analytical work [8] we label even and odd-parity modes with $\epsilon = 0$ and $\epsilon = 1$, while in Eq. (3) above we used the labelling (e) and (o).

The insplumerg waveform can be written as the product of several factors. We factorize the NQC correction as

$$h_{\ell m}^{\text{insplumerg }(\epsilon)}(t; a_i^{\ell m}) = h_{\ell m}^{\text{insplunge}(\epsilon)} h_{\ell m}^{\text{NQC}}(a_i), \quad (6)$$

and the *insplunge waveform* is given as the product of the Newtonian contribution and a PN (resummed) correction by

$$h_{\ell m}^{\text{insplunge }(\epsilon)} \equiv h_{\ell m}^{(N,\epsilon)}(x) \hat{h}_{\ell m}^{(\epsilon)}. \quad (7)$$

The Newtonian contribution is given by

$$h_{\ell m}^{(N,\epsilon)} = \frac{M\nu}{\mathcal{R}} n_{\ell m}^{(\epsilon)} c_{\ell+\epsilon}(\nu) x^{(\ell+\epsilon)/2} Y^{\ell-\epsilon,-m}\left(\frac{\pi}{2}, \varphi\right), \quad (8)$$

where $Y^{\ell m}(\theta, \phi)$ are the usual scalar spherical harmonics (computed on the equatorial plane $\theta = \pi/2$), and the numerical coefficients $n_{\ell m}^{(\epsilon)}$ and $c_{\ell+\epsilon}(\nu)$ are explicitly given by Eqs. (5)-(7) of Ref. [8]. Because we work here in the EMRL ($\nu \to 0$), we pose $c_{\ell+\epsilon}(0)$, leaving only the overall factor ν. Following Ref. [6] (consistently with Ref. [29, 55]), the argument x in the Newtonian prefactor of Eq. (7) is taken as

$$x = v_\varphi^2 = (r\Omega)^2 \ , \quad (9)$$

where Ω is the orbital frequency. This choice is preferable to $x = x_{\text{circ}} \equiv \Omega_{\text{circ}}^{2/3}$. due to the violation of circular Kepler's law during the plunge phase. The quantity

$$\hat{h}_{\ell m}^{(\epsilon)} \equiv \hat{S}_{\text{eff}}^{(\epsilon)} T_{\ell m} e^{\mathrm{i}\delta_{\ell m}} (\rho_{\ell m})^\ell \quad (10)$$

represents a factorized (and resummed) version of all the PN corrections to the waveform. It is given as the product of four factors: the μ-normalized effective source $\hat{S}_{\text{eff}}^{(\epsilon)}$, the tail factor $T^{\ell m}$ that resums an infinite number of leading logarithms entering the *tail effects*, the supplementary phase $\delta_{\ell m}$, and the residual modulus correction $\rho_{\ell m}$. The even-parity effective source, $\hat{S}_{\text{eff}}^{(0)}$, is given by the μ-normalized Hamiltonian of the system computed along the dynamics, while the odd-parity one, $\hat{S}_{\text{eff}}^{(1)}$, is given by the corresponding (Newton-normalized) angular momentum. The explicit expression of the tail factor as a function of the orbital frequency Ω reads

$$T_{\ell m}(\Omega) = \frac{\Gamma(\ell + 1 - 2\mathrm{i}\hat{\hat{k}})}{\Gamma(\ell+1)} e^{\pi\hat{\hat{k}}} e^{2\mathrm{i}\hat{\hat{k}}\ln(2kr_{0s})}, \quad (11)$$

where $k = m\Omega$, $\hat{\hat{k}} = Mk$. Following [46], we denote by r_{0s} the quantity that was previously denoted as r_0 in [8], and we choose $r_{0s} = r_0 = 2M/\sqrt{e}$ for consistency between the computations of the phase of [46] and [8]. This value is chosen to match PN results (in harmonic coordinates) with black-hole perturbation results in Schwarzschild coordinates used here.

Finally, the factor $h_{\ell m}^{\text{NQC}}(a_i^{\ell m})$ is a correction that models the noncircular effects in the waveform. This effective term allows us to analytically compute the waveform beyond the circular approximation. The necessity of using a NQC corrective factor to the waveform *amplitude* (usually denoted as f^{NQC}), was first pointed out in [29] and then used (with variations) in several studies [3, 4, 6, 7, 10]. The inclusion of such NQC correction proved necessary to improve the closeness of the $m = \ell = 2$ EOB waveform to the numerical one during the late-plunge and merger dynamics. Building on this knowledge we extend the use of h_{22}^{NQC} [6, 29] to the other multipoles, with the important difference that we consider also corrections to the waveform *phase* [7, 29]. This generalized NQC factor takes the form

$$h_{\ell m}^{\text{NQC}}(a_i^{\ell m}) = \left(1 + a_1^{\ell m}\frac{p_{r_*}^2}{(r\Omega)^2} + a_2^{\ell m}\frac{\ddot{r}}{r\Omega^2}\right) \times \exp\left[\mathrm{i}\left(a_3^{\ell m}\frac{p_{r_*}}{r\Omega} + a_4^{\ell m}\frac{\dot{\Omega}}{\Omega^2}\right)\right], \quad (12)$$

where the $a_i^{\ell m}$'s are NQC flexibility parameters that have to be determined, multipole by multipole, by imposing some compatibility conditions between the EOB and RWZ waveforms around the merger time.

IV. COMPARING EOB AND RWZ WAVEFORMS

In this section we present the comparison between RWZ and EOB waveforms. In the first part we assess the performances of the resummed *insplunge waveform*, Eq. (7), to describe the inspiral up to the LSO crossing. The insplunge waveform includes neither NQC corrections nor matching to QNMs. Nonetheless it shows a very good agreement with RWZ during the whole inspiral up to (and even below) the LSO. In the second part we focus on the transition from inspiral to plunge, merger and ringdown, and we compare to the RWZ waveform the three different analytical representations of the resummed multipolar waveform introduced above. Specifically we consider the same insplunge waveform mentioned above; the *insplumerg waveform* that includes only the NQC corrections (to both phase and amplitude), Eq. (6); and the full EOB waveform, Eq. (4), with NQC corrections and with QNMs matching. We emphasize the necessity of introducing NQC corretions to the resummed EOB waveform and we propose compatibility conditions with the RWZ waveform to determine the NQC parameters $a_i^{\ell m}$. The procedure we discuss is equally robust for all multipoles and does not require any relative time and phase shifting of the waveforms, or any hand-tuning of parameters.

We present our comparison consistently with the notation of Paper I, *i.e.* we use "Zerilli-normalized" metric multipoles $\Psi_{\ell m}$. These are related to the $\mathcal{R}h_{\ell m}$ metric

TABLE I. Phase difference $\Delta\phi^{\rm insplunge} \equiv \phi^{\rm EOB}_{\ell m} - \phi^{\rm RWZ}_{\ell m}$ and relative amplitude difference $(\Delta A/A)^{\rm insplunge} = (A^{\rm EOB}_{\ell m} - A^{\rm RWZ}_{\ell m})/A^{\rm RWZ}_{\ell m}$ between insplunge EOB and RWZ waveforms computed at $t_0 = 500M$ and at the LSO crossing, $t_{\rm LSO} = 4076.1M$, for all the $(m \neq 0)$ multipoles with $2 \leq \ell \leq 4$.

ℓ	m	$\Delta\phi^{\rm insplunge}_{500M}$	$\Delta\phi^{\rm insplunge}_{\rm LSO}$	$(\Delta A/A)^{\rm insplunge}_{500M}$	$(\Delta A/A)^{\rm insplunge}_{\rm LSO}$
2	1	-3.91 $\times 10^{-4}$	-4.04$\times 10^{-3}$	-1.16$\times 10^{-4}$	-9.62$\times 10^{-4}$
2	2	4.16 $\times 10^{-4}$	-2.48$\times 10^{-3}$	-1.40$\times 10^{-3}$	-2.72$\times 10^{-3}$
3	1	-1.74 $\times 10^{-3}$	-1.86$\times 10^{-2}$	-5.56$\times 10^{-4}$	-4.6$\times 10^{-3}$
3	2	-3.29 $\times 10^{-4}$	-4.65$\times 10^{-3}$	7.54$\times 10^{-4}$	9.54$\times 10^{-4}$
3	3	3.19 $\times 10^{-4}$	-3.76$\times 10^{-3}$	-1.98$\times 10^{-3}$	-4.10$\times 10^{-3}$
4	1	-2.06 $\times 10^{-3}$	-2.36$\times 10^{-2}$	-2.96$\times 10^{-4}$	-8.02$\times 10^{-3}$
4	2	-1.35 $\times 10^{-3}$	-1.51$\times 10^{-2}$	-9.55$\times 10^{-4}$	-3.98$\times 10^{-3}$
4	3	2.78 $\times 10^{-3}$	5.69$\times 10^{-4}$	1.15$\times 10^{-3}$	1.80$\times 10^{-3}$
4	4	4.22 $\times 10^{-4}$	-4.40$\times 10^{-3}$	3.42$\times 10^{-3}$	7.1$\times 10^{-3}$

multipoles as

$$\Psi^{{\rm X},(\epsilon)}_{\ell m} = {\rm i}^{\epsilon} N_\ell \mathcal{R} h^{{\rm X}(\epsilon)}_{\ell m}, \tag{13}$$

where $N_\ell = 1/\sqrt{(\ell+2)(\ell+1)\ell(\ell-1)}$ and the label X stays for either insplunge, insplumerg, or EOB. Note that this convention implies a phase shift of $\pi/2$ between the odd-parity multipoles $\mathcal{R}h^{(1)}_{\ell m}$ and $\Psi^{(1)}_{\ell m}$. The EOB and RWZ multipolar waveforms are computed from the same dynamics; the RWZ one is typically extracted at $\mathcal{I}^+$ and shown versus the corresponding retarded time $\tau - S$. The EOB waveforms is parametrized by the dynamical time t, that will always be used as reference time axis. Finally, the phases, $\phi_{\ell m}$, and the amplitudes, $A_{\ell m}$, of the (RWZ or EOB) complex numbers $\Psi_{\ell m}$ are defined with the convention $\Psi_{\ell m} = A_{\ell m} e^{-{\rm i}\phi_{\ell m}}$.

A. Quasi-adiabatic inspiral

Let us focus first on the quality of the resummed waveform during the long (~ 37 orbits) quasi-adiabatic inspiral. We identify here the end of the inspiral (and the beginning of the plunge) as the time $t_{\rm LSO} = 4076.2M$ at which the particle crosses the last stable orbit $r_{\rm LSO} = 6M$. This is clearly a convention because the transition from the inspiral to plunge is a blurred process that occurs around $r_{\rm LSO}$ [18, 19, 56].

The upper panel of Fig. 2 displays the early-time evolution of the real part of the $\ell = 2$ EOB multipoles (dashed lines) (top, $m = 1$, bottom $m = 2$) together with the RWZ ones (solid lines). After the initial unphysical transient the plot shows a remarkably good agreement between phases and amplitudes of the two waveforms. The time-evolution of the corresponding phase differences (during the complete inspiral) $\Delta\phi^{\rm EOBRWZ}_{\ell m}(t) = \phi^{\rm EOB}_{\ell m}(t) - \phi^{\rm RWZ}_{\ell m}(t)$, is shown (as thicker lines, red online)

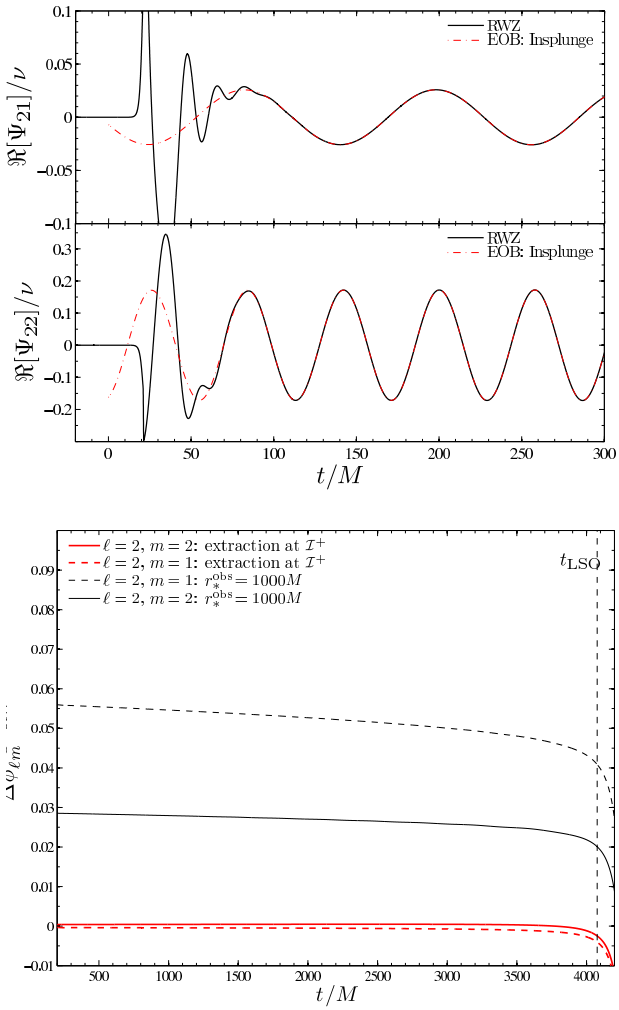

FIG. 2. Testing the waveform resummation for $\ell = 2$ at the beginning of the inspiral. Top panel: insplunge and RWZ waveforms extracted at $\mathcal{I}^+$. Bottom panel: the phase differences $\Delta\phi^{\rm EOBRWZ}_{\ell m} = \phi^{\rm EOB}_{\ell m} - \phi^{\rm RWZ}_{\ell m}$, for RWZ waveforms measured at $\mathcal{I}^+$, are contrasted with the corresponding ones for RWZ waveforms measured at a finite extraction radius, $r^{\rm obs}_* = 1000M$.

in the lower panel of Fig. 2. The vertical dashed-line in the lower panel of the figure (with label $t_{\rm LSO}$) indicates the LSO-crossing time. At the beginning, say for $t/M < 500$ (first 4 orbital cycles), the magnitude of both $\Delta\phi^{\rm EOBRWZ}_{22}(t)$ and $\Delta\phi^{\rm EOBRWZ}_{21}(t)$ is below 10^{-3}. More precisely, at $t = t_0 = 500M$, we have $\Delta\phi^{\rm EOBRWZ}_{22}(t_0) = 4.16 \times 10^{-4}$ and $\Delta\phi^{\rm EOBRWZ}_{21}(t_0) = -3.98 \times 10^{-4}$. Such a small dephasing is compatible with the expected uncertainty on the 4.5PN-accurate phases $\delta_{\ell m}$ in Eq. (10). By evaluating the last (the 4.5PN ones) terms in Eqs. (5.8a)-(5.8b) of [46] at the initial position $r_0 = 7M$, we estimate $\delta^{\rm 4.5PN}_{22} \sim 4.16 \times 10^{-3}$ and $\delta^{\rm 4.5PN}_{21} \sim 5.27 \times 10^{-4}$. Even if the phase difference grows by an order of magnitude on the interval $[t_0, t_{\rm LSO}]$, it remains small at $t_{\rm LSO}$. Table I accounts for the complete information, multipole by mul-

tipole, about phase and fractional amplitude differences, $(\Delta A/A)_{\ell m} = (A^{\rm EOB}_{\ell m} - A^{\rm RWZ}_{\ell m})/A^{\rm RWZ}_{\ell m}$, both at t_0 and at $t_{\rm LSO}$.

When we sum together all the multipoles in the complete waveform, Eq. (3), we initially obtain $\Delta\phi^{\rm insplunge}_{500M} = 5\times10^{-4}$ (corresponding to total GW phase $\phi = 51.74$ rad), that becomes as large as -2×10^{-3} at the LSO ($\phi = 472.1$ rad). This means that the complete EOB insplunge waveform has dephased from the numerical one by only about -2.5×10^{-3} rad over the ~ 420 rad (~ 33 orbits) of GW phase evolution on the interval $[t_0, t_{\rm LSO}]$, which yields $\Delta\phi^{\rm EOBRWZ}/\phi^{\rm RWZ} = -5.95\times10^{-6}$.

We point to one of the main findings of Ref. [48] in the lower panel of Fig. 2. The figure depicts the phase differences to numerical waveforms extracted at the *finite radius*[3] $r^{\rm obs}_* = 1000M$ and displayed versus the corresponding observer retarded time. The plot clearly shows that the values of $\Delta\phi^{\rm EOBRWZ}_{\ell m}$ obtained with waves extracted at a finite radius (though very large) are approximately two orders of magnitude larger than those obtained with waves extracted at null infinity. The phenomenon discussed here in the $\ell = 2$ case remains the same for the other multipoles. In particular, the largest and the smallest dephasing is for the $m = 1$ and the $m = \ell$ multipoles respectively. The dephasing might grow (up to the ~ 0.1 rad level) for $\ell > 2$. The small dephasing of the waveform from the hyperboloidal layer calculation is the result of accurate wave extraction at null infinity [48]. At the present stage, this simple plot teaches us a very useful lesson: extracting waves at $1000M$, even in the EMRL, may introduce dephasings that are considerably *larger* than the ones expected on the basis of the analytical knowledge of the GW phase. A priori one expects such phenomenon to be equally relevant, or even more important, in the comparable mass-ratio case due to the smaller PN-accuracy at which the $\delta_{\ell m}$'s are known when $\nu \neq 0$ [8].

B. Compatibility conditions at merger

Let us focus now on the late-time part of the waveform corresponding to plunge, merger and ringdown, *i.e.* $t > t_{\rm LSO}$. The discussion mainly focusses again on the $\ell = 2$ modes as a paradigmatic example. The relevant information is collected in Fig. 3. The top panels show the various waveform moduli divided by ν, *i.e.* $A_{2m}/\nu \equiv |\Psi_{2m}|/\nu$, with self-explanatory labelling. The bottom panels show the corresponding instantaneous GW frequencies $M\omega_{2m} = -\Im\left(\dot\Psi_{\ell m}/\Psi_{\ell m}\right)$. For reference also the orbital frequency $M\Omega$ is depicted on all panels. The vertical dashed line indicates the location of the maximum of Ω at $t = t_{\Omega_{\rm max}} = 4308.4M$, that corresponds to the time $t = t_{\rm LR}$ when the particle crosses the light-ring $r_{\rm LR} = 3M$. Note again that we do not allow for any arbitrary time or phase-shift between EOB and RWZ quantities.

TABLE II. Strong-field-fast-motion information from the RWZ waveform at the light-ring crossing $t = t_{\rm LR} = 4308.4M$ and used to determine the $a_i^{\ell m}$ coefficients via the conditions given by Eqs. (14)-(17).

ℓ	m	$A_{\ell m}(t_{\rm LR})/\nu$	$A_{\ell m}(t_{\rm LR})/\nu$	$M\omega_{\ell m}(t_{\rm LR})$	$M\dot\omega_{\ell m}(t_{\rm LR})$
2	1	0.945×10^{-1}	0.271×10^{-2}	0.195×10^{-0}	0.867×10^{-2}
2	2	0.293×10^{-0}	-0.157×10^{-2}	0.288×10^{-0}	0.630×10^{-2}
3	1	0.359×10^{-2}	0.238×10^{-3}	0.250×10^{-0}	0.126×10^{-1}
3	2	0.159×10^{-1}	0.496×10^{-3}	0.350×10^{-0}	0.132×10^{-1}
3	3	0.514×10^{-1}	0.152×10^{-3}	0.443×10^{-0}	0.106×10^{-1}
4	1	0.187×10^{-3}	0.221×10^{-4}	0.321×10^{-0}	0.223×10^{-1}
4	2	0.118×10^{-2}	0.647×10^{-4}	0.405×10^{-0}	0.191×10^{-1}
4	3	0.424×10^{-2}	0.152×10^{-3}	0.499×10^{-0}	0.171×10^{-1}
4	4	0.143×10^{-1}	0.146×10^{-3}	0.592×10^{-0}	0.144×10^{-1}

As previously observed [29] the modulus of the insplunge $m = 2$ waveform (left panel of Fig. 3) is in very good agreement during the complete inspiral and during most of the plunge phase, while overshooting the numerical one by about 10% around $t_{\rm LR}$. The frequency is indistinguishable by eye up to $t \approx 4240$ (relative error of 0.5%), whereas it clearly underestimates the numerical one later on (by 11% at $t_{\rm LR}$). Similar results hold for the frequency of the $m = 1$ multipole. In this case, however, the insplunge amplitude is slightly smaller than the numerical one at $t_{\rm LR}$.

As discussed in Sec. III, a way to improve the insplunge waveform in the strong-field-fast-motion regime is to include the NQC corrections, *i.e.* to consider the insplumerg waveform, Eq. (6). The insplumerg waveform depends on the $a_i^{\ell m}$ parameters that must be tuned requiring some compatibility conditions with the numerical waveform. Previous work [6, 7, 10, 29] was mostly restricted to the quadrupolar $m = \ell = 2$ waveform and considered only NQC amplitude corrections, *i.e.* fixed $a_3^{22} = a_4^{22} = 0$ by construction in Eq. (6) (see, however, Ref. [10] for a preliminary investigation of the effect of a_3^{22} for spinning binaries). The amplitude-related parameters in $h^{\rm NQC}_{\ell m}$ were generically fixed by imposing that: (i) the maximum of the EOB waveform amplitude occurs at the time when the EOB orbital frequency peaks, $t_{\Omega_{\rm max}}$; (ii) the maxima of the EOB and the numerical waveforms amplitude agree at $t_{\Omega_{\rm max}}$. When only two parameters are present [6], these conditions are sufficient to fix $a_i^{\ell m}$ with

[3] We checked this result also using the numerical setup of Paper I, *i.e.* with evolution along Cauchy time surfaces on a finite-size r_* domain $r_* \in [-500, 1500]$ and artificial boundaries (with Sommerfeld's outgoing boundary conditions) instead of a hyperboloidal layer. A thorough discussion of these effects will be given in Ref. [48].

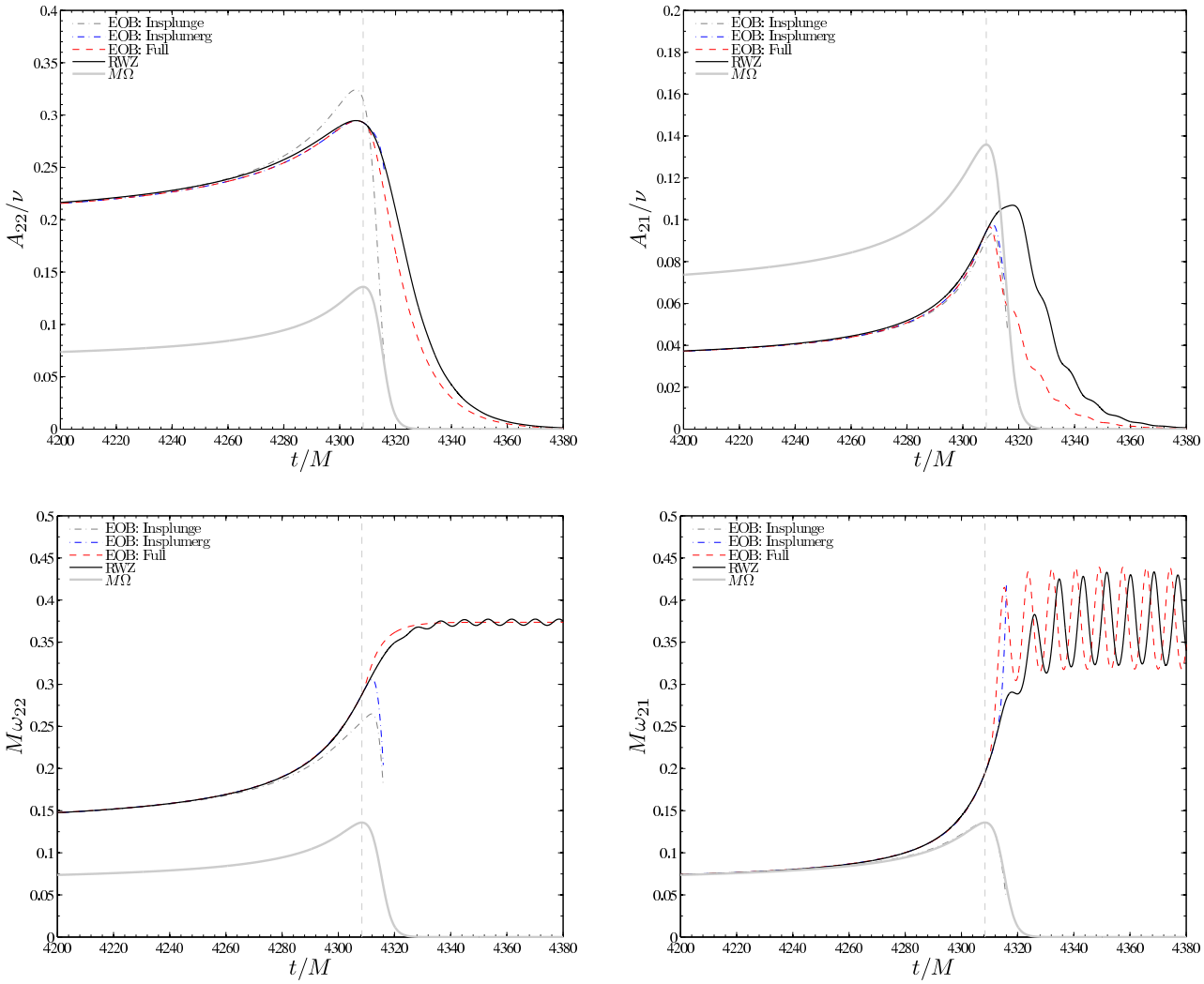

FIG. 3. Addition of NQC corrections and matching to QNMs; $\ell = 2$ multipoles. The (light) dashed lines refer to the bare insplunge waveform, without the addition of NQC corrections (dash-dotted, blue online) nor of QNM ringdown (dashed, red online). The vertical (light) dashed-line indicates the location of the maximum of $M\Omega$.

$i = 1, 2$. Additional parameters are tuned by locally fitting the numerical waveform [7, 10]. Our procedure builds upon previous works [6, 29] with important differences. First, we take into account both phase corrections in Eq. (12). The need for NQC phase corrections is motivated the frequency plots in Fig. 3 (note the rather large "gap" between the RWZ and the EOB insplunge frequencies at $t_{\rm LR}$), and requires two more conditions to fix the $a_i^{\ell m}$ parameters with $i = 3, 4$. Second, we determine the four parameters $a_i^{\ell m}$ by demanding agreement of EOB and RWZ waveforms in amplitude, frequency, and their first derivatives at a given time $t = t_m$. Third, the procedure is applied to all multipoles. In formulae, our conditions read:

$$A_{\ell m}^{\rm EOB}(t_m) = A_{\ell m}^{\rm RWZ}(t_m), \tag{14}$$
$$\dot{A}_{\ell m}^{\rm EOB}(t_m) = \dot{A}_{\ell m}^{\rm RWZ}(t_m), \tag{15}$$
$$\omega_{\ell m}^{\rm EOB}(t_m) = \omega_{\ell m}^{\rm RWZ}(t_m), \tag{16}$$
$$\dot{\omega}_{\ell m}^{\rm EOB}(t_m) = \dot{\omega}_{\ell m}^{\rm RWZ}(t_m). \tag{17}$$

The necessary information extracted from the RWZ waveform is displayed in Table II. The only remaining freedom in this procedure is the choice of t_m. According to the usual EOB prescription we choose it from the EOB dynamics as the time $t_{\Omega_{\rm max}}$ when the orbital frequency peaks, *i.e.* the time when the small BH crosses the light-ring at $3M$. In our setting we have $t_m = t_{\rm LR} = t_{\Omega_{\rm max}} = 4308.4M$. We note that $t_{\rm LR}$ does not exactly coincide with the time locations, $t_{\rm max}^{\ell m}$, of the peaks of the $A_{\ell m}$'s. In particular A_{22} peaks $2.56M$ *earlier* than $t_{\rm LR}$, while A_{21}

peaks $9.40M$ *later*. Thus the maxima of the amplitude of the multipolar waveform have no strict relation with the light-ring crossing, but they remain clearly identifiable points in the waveforms. An analysis of the amplitude maxima is reported in Appendix B. The information in Fig. 3 is completed by Table VI in Appendix B. The third column of the table lists the time shift, $t^{\ell m}_{\rm max} - t_{\rm LR}$, with respect to the light-ring crossing, $t_{\rm LR}$, at which each multipolar amplitude peaks.

The $\ell = 2$ insplumerg amplitudes and frequencies with NQC parameters determined from Eqs. (14)-(17) are shown as dash-dotted lines (blue online) in Fig. 3. The insplumerg is very effective in reproducing the numerical data. The corresponding maximum phase difference accumulated between $t_{\rm LSO}$ and $t_{\rm LR}$ amounts to 0.025 rad for both multipoles, and the maximum relative difference in amplitude is below 2% (see also Figs. 4 and 5 below).

The complete EOB amplitude and frequencies with the QNM contribution matched at $t_{\rm LR}$ are shown as dashed-line (red online) in the four panels of Fig. 3 (labeled as EOB: Full). We match both multipoles to three QNMs, using the values computed in [57]. For $m = 2$ we use three positive frequency modes, σ^{+}_{n2}, with $n = (0, 1, 2)$ and we neglect the negative-frequency mode contribution because it is very small [45]. For $m = 1$ we use two positive frequency modes, σ^{+}_{n2}, with $n = (0, 1)$ and one negative mode σ^{-}_{02}, to qualitatively reproduce the related oscillation in $M\omega_{21}$. The center of the 3-point matching interval $[t_m - \Delta/2, t_m + \Delta/2]$ ("comb") is chosen $t_m = t_{\rm LR}$ and its width is $\Delta = M$. The matching procedure is robust for different choices of Δ and employs a minimum number of QNMs. A larger matching interval [29] does not yield any improvement in the current setting, while a pointwise matching ($\Delta \to 0$) leads to inaccurate results. From the figure it is clear that the representation of the ringdown does capture the behavior of the numerical waveform more accurately in the $m = 2$ case and less accurately in the $m = 1$ case. This is a consequence of two facts. First, in the EOB framework the transition from merger to QNM ringdown is localized, by construction, at one single point $t = t_m$. Second, we choose to determine the NQC parameters and to match to QNMs at the same time, namely $t_m = t_{\rm LR}$. We have explored in Appendix A the possibility of matching QNMs at a shifted time (common to all multipoles) $t_{\rm match} > t_{\rm LR}$, while keeping the tuning of NQC corrections fixed at $t_{\rm merger} = t_{\rm LR}$. The agreement of modulus, frequency, and phase during ringdown significantly improves for all multipoles, at the price, however, of one arbitrary shift parameter, namely $\Delta t = t_{\rm match} - t_{\rm merger}$.

V. COMPLETE MULTIPOLAR WAVEFORM

In this section we evaluate the performance of the procedure discussed above to determine the NQC parameters a_i when it is applied to the other multipoles with $\ell > 2$. In the end we put together all the multipolar information to obtain the complete $\mathcal{R}(h_+ - {\rm i}h_\times)$ waveform given by Eq. (3).

TABLE III. Values of the NQC coefficients $a_i^{\ell m}$ entering the $h^{\rm NQC}_{\ell m}$ factor, Eq. (12). These numbers are obtained imposing the compatibility conditions Eqs. (14)-(17) between EOB and RWZ waveforms at $t = t_m$.

ℓ	m	$a_1^{\ell m}$	$a_2^{\ell m}$	$a_3^{\ell m}$	$a_4^{\ell m}$
2	1	0.0316	-0.2874	0.7682	-0.5872
2	2	0.0173	0.9782	0.5019	-0.4739
3	1	2.8720	-8.4234	1.5859	-1.3737
3	2	-0.0043	0.4691	1.0368	-0.7618
3	3	0.0722	0.9354	0.7202	-0.5865
4	1	5.0865	-23.6007	2.5108	-2.0970
4	2	1.8166	-4.5120	1.7064	-1.2990
4	3	0.0058	0.8158	1.1501	-0.7671
4	4	0.1120	1.3162	0.9295	-0.7227

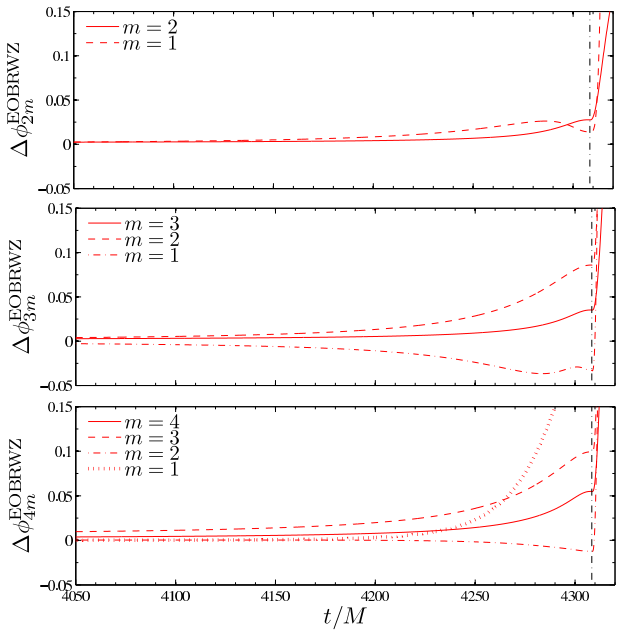

FIG. 4. Time evolution of the phase difference $\Delta\phi^{\rm EOBRWZ}_{\ell m} = \phi^{\rm EOB}_{\ell m} - \phi^{\rm RWZ}_{\ell m}$ between full EOB and RWZ multipolar waveforms. The dash-dotted vertical line locates the light-ring.

A. Multipoles with $\ell > 2$

The qualitative behavior of the insplunge waveform during the late-plunge phase for $\ell > 2$ is analogous to the $\ell = 2$ case. The $m = \ell$ EOB waveform amplitude is always slightly larger than the corresponding numerical one around merger, and progressively smaller when

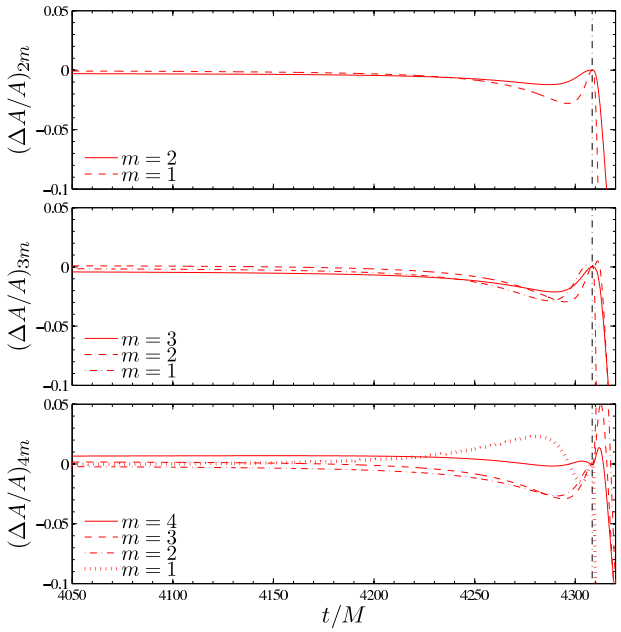

FIG. 5. Time evolution of the relative amplitude difference $(\Delta A/A)_{\ell m} = (A^{\rm EOB}_{\ell m} - A^{\rm RWZ}_{\ell m})/A^{\rm RWZ}_{\ell m}$ between full EOB and RWZ multipolar waveforms. The dash-dotted vertical line locates the light-ring.

TABLE IV. Phase difference $\Delta\phi^{\rm EOB} \equiv \phi^{\rm EOB}_{\ell m} - \phi^{\rm RWZ}_{\ell m}$ and relative amplitude difference $(\Delta A/A)^{\rm EOB} \equiv (A^{\rm EOB}_{\ell m} - A^{\rm RWZ}_{\ell m})/A^{\rm RWZ}_{\ell m}$ between the full EOB and RWZ waveforms computed at $t_0 = 500M$ and at the LSO crossing, $t_{\rm LSO} = 4076.1M$, for all the $(m \neq 0)$ multipoles with $2 \leq \ell \leq 4$.

ℓ	m	$\Delta\phi^{\rm EOB}_{500M}$	$\Delta\phi^{\rm EOB}_{\rm LSO}$	$(\Delta A/A)^{\rm EOB}_{500M}$	$(\Delta A/A)^{\rm EOB}_{\rm LSO}$
2	1	2.49×10^{-4}	2.95×10^{-3}	-1.15×10^{-4}	-8.66×10^{-4}
2	2	8.79×10^{-4}	2.56×10^{-3}	-1.40×10^{-3}	-3.04×10^{-3}
3	1	-3.3×10^{-4}	-3.35×10^{-3}	-5.42×10^{-4}	-1.75×10^{-3}
3	2	5.18×10^{-4}	4.62×10^{-3}	7.54×10^{-4}	7.98×10^{-4}
3	3	9.37×10^{-4}	2.98×10^{-3}	-1.98×10^{-3}	-4.40×10^{-3}
4	1	1.19×10^{-4}	2.04×10^{-4}	-2.57×10^{-4}	-1.34×10^{-4}
4	2	6.6×10^{-5}	3.67×10^{-4}	-9.48×10^{-4}	-2.45×10^{-3}
4	3	3.68×10^{-3}	1.04×10^{-2}	1.15×10^{-3}	1.53×10^{-3}
4	4	1.20×10^{-3}	4.12×10^{-3}	3.41×10^{-3}	6.70×10^{-3}

$1 \leq m < \ell$. Analogously, the gap between RWZ and EOB frequency is always smaller when $m = \ell$ and progressively larger when m decreases. This suggests that one should obtain numerical values for the $a^i_{\ell m}$ coefficients that are systematically larger when m decreases, as we actually find (see Table III). Note in addition that the value of a^{22}_2 is of order unity, while that of a^{22}_1 is of order 10^{-2} (as well as most of the others). These numerical values indicate the consistency of the procedure when it is applied to the EMRL case or to the comparable mass case. Following values were obtained in [6]: $a^{22}_1 = -0.036347$ and $a^{22}_2 = 1.2468$ in the equal-mass case ($\nu = 1/4$), and $a^{22}_1 = -0.017017$ and $a^{22}_2 = 1.1906$ in the 2:1 mass case ($\nu = 2/9$). The variation of the coefficients a^{22}_i is mild when ν varies between 0 and 1/4, and it indicates that most of the ν-dependence is already accounted for by the linear momentum p_{r_*} and its first time derivative. It will be interesting to investigate whether this consistency remains (and at what accuracy) for the other multipoles.

Figures 4 and 5 quantify the phase differences $\Delta\phi^{\rm EOBRWZ}_{\ell m}$ as well as the relative amplitude difference $(\Delta A/A)_{\ell m}$ for all multipoles. These quantities remain quite small until the light-ring: $\max(\Delta\phi^{\rm EOBRWZ}_{\ell m}) \lesssim 0.15$ rad and $|(\Delta A/A)_{\ell m}| \lesssim 2.5\%$. Table IV (that is the analogue of Table I) completements the late-time information given by Figs. 4 and 5 by listing the numerical values of the phase difference and the relative amplitude difference at $t_0 = 500M$ and at the LSO crossing. The accuracy obtained until the light-ring is then lost during the ringdown part, especially for subdominant multipoles. Because we are determining the NQC phase-correction parameters $(a^{\ell m}_3, a^{\ell m}_4)$ by means of one condition on $\omega = \dot\phi$ and one on $\dot\omega_{\ell m} = \ddot\phi_{\ell m}$, the phase difference itself *is not* exactly zero at the matching point $t_m = t_{\rm LR}$ (as it is the case for the amplitude difference). This choice of imposing compatibility on $\omega_{\ell m}$ and $\dot\omega_{\ell m}$ might look overcomplicated: one could just impose compatibility of the phase and its first time derivative. Working only with derivatives of the phase may allow us to extend our procedure to the comparable mass case using NR data to tune the NQC corrections. While in this work we have an unambiguous correspondence between the dynamics and the numerical waveform, in the NR simulation this is not the case: the dynamics is not evidently available and one must typically rely only on waveform information that comes with some arbitrary initial phase. A procedure to fix $(a^{\ell m}_3, a^{\ell m}_4)$ independently of the GW phase is then preferable. In this respect Fig. 4 indicates that compatibility conditions on $\omega_{\ell m}$ and $\dot\omega_{\ell m}$ effectively yield phase differences that are quite small at the matching point (especially for the $m = \ell$ multipoles). As we shall see in the next section, the larger phase differences that are obtained for subdominant multipoles at t_m (like the (4,1) case) have no practical influence on the complete waveform.

Finally we tested the procedure by using as matching time the location of the maximum of the $m = \ell = 2$ amplitude $t^{22}_{\rm max}$, that occurs $2.56M$ before $t_{\rm LR}$. We measured the corresponding values of the RWZ functions and computed the NQC correction factors accordingly. Because $t^{22}_{\rm max} \simeq t_{\rm LR}$, the EOB waveforms obtained in this way are fully compatible with those shown so far. Moreover, we also explored the effect of using a different matching time for each multipole, *i.e.* using as t_m the location of the maxima of the various $A_{\ell m}$. For some multipoles this procedure is very effective in obtaining an accurate representation of the modulus, like for example in the $(2,1)$

or $(3,1)$ case, although it typically fails to reproduce the frequency. The reason for this is that in several situation the matching position already corresponds to the final growth of the frequency and the simple representation given by our NQC corrections does not capture the correct behavior there. Therefore, we prefer to use the simple procedure discussed so far, even if it might lead to a relatively inaccurate representation of the ring-down part of the amplitude for certain multipoles (as for $\ell = 2$, $m = 1$).

B. The complete $h_+ - \mathrm{i}h_\times$ waveform

Now that we have assessed the quality of the EOB representation of the higher-order multipoles, let us compare the RWZ and complete EOB gravitational waveforms. This comparison is shown in Figs. 6 and 7. Figure 6 displays the late-time evolution of the two GW polarizations, $\mathcal{R}h_+/\nu$ (top) and $\mathcal{R}h_\times/\nu$ (bottom), that are computed by summing together all the $m \neq 0$ multipoles up to $\ell = 4$ using Eq. (3) and considering a fiducial direction of emission $(\theta, \Phi) = (\pi/4, 0)$. The corresponding phase difference is shown in Fig. 7. At the beginning of the inspiral (top panel) the dephasing is as small as 1×10^{-3} rad and is seen to progressively increase up to only 4×10^{-3} rad at the LSO crossing (dashed vertical line). The phase difference increases then by an order of magnitude during the plunge phase and reaches about 0.03 rad at the light-ring crossing (dash-dotted vertical line). The main contribution to the phase difference comes from the $\ell = 2$ modes and the $m = \ell$ modes with $\ell > 2$. The other modes have a much smaller impact (especially around merger), even in the EMRL. The relatively rough description of the ringdown structure (especially for the $\ell = 2$, $m = 1$ mode) implies that the phase difference is larger after the light-ring crossing, though it is mainly oscillating around zero.

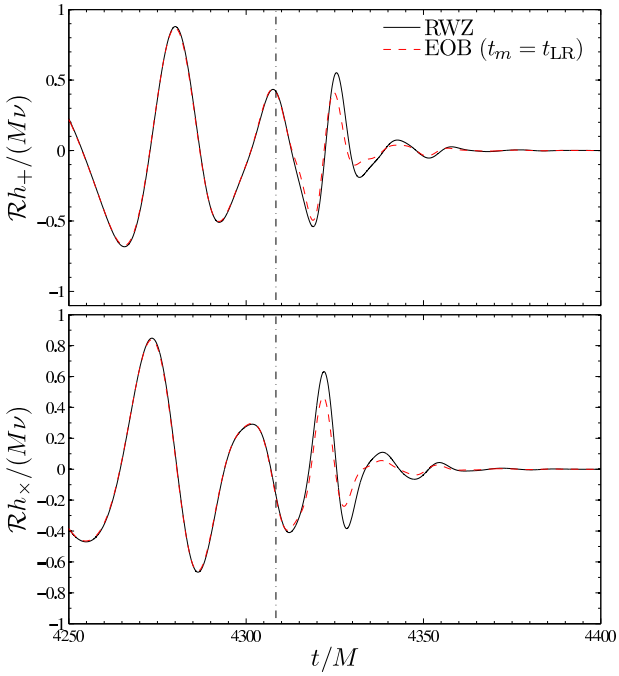

FIG. 6. Comparison between RWZ and EOB complete gravitational waveforms taken in the direction $(\theta, \Phi) = (0, \pi/4)$. The two panels show the time-evolution of the two polarizations $(h_+, h_\times)$ computed including up to $\ell = 4$ multipoles for $\nu = 10^{-3}$ (the $m = 0$ multipoles are neglected).

VI. CONCLUSIONS

In this paper we have discussed the properties of the gravitational radiation emitted during the transition from quasicircular inspiral to plunge of two nonspinning black-holes in the EMRL within the EOB framework. We considered for the first time the whole multipolar structure of EOB-resummed waveforms and we compared and calibrated them against recently calculated Regge-Wheeler-Zerilli numerical waveforms [45, 48]. The target numerical waveforms are extracted at null infinity via the hyperboloidal layer method [48–51]. The binary dynamics is modeled in both cases for a point-particle moving on a Schwarzschild background under the action of $\mathcal{O}(\nu)$ dissipative radiation reaction force computed using analytically resummed 5PN results [8, 46]. As a paradigmatic example, we have considered a binary with mass ratio $\nu = 10^{-3}$, initially at a relative separation of $7M$, that inspirals for about 37 orbits before plunging into the black hole. The setup of our point-particle "laboratory" is sufficiently general to allow us to gather information that can be useful both in the analytical models of waveforms emitted by EMRI (target sources for LISA) as well as for the coalescence of comparable mass black holes (target sources for ground-based interferometers). Our results can be summarized as follows.

Quasi-adiabatic inspiral. At the beginning of the inspiral, the phase difference between the complete EOB and RWZ waveforms (computed without allowing for any relative time and phase shift) is very small, $\Delta\phi^{\rm EOBRWZ} \sim 5 \times 10^{-4}$ rad. This value is consistent with the estimated uncertainty related to the residual phases $\delta_{\ell m}$ entering the EOB waveform known only up to 4.5PN level. During the ~ 33 orbits of the inspiral after the junk radiation ($t < 500M$) up to the LSO crossing (corresponding to ~ 420 radians of total GW phase) the system accumulates only -2.5×10^{-3} radians, *i.e.* $\Delta\phi^{\rm EOBRWZ}/\phi^{\rm RWZ} = -5.95 \times 10^{-6}$. Such remarkable phase coherence, that is obtained with the EOB insplunge waveform —without any tunable parameter— strongly indicates the aptitude of EOB waveforms to model EMRIs for LISA.

Our conclusions are compatible with those of Refs. [30, 31] although there are two important differences. First, our two waveforms are computed from the same dynamics in order to focus *only* on waveform comparison so to test the efficiency of the resummation of the EOB wave-

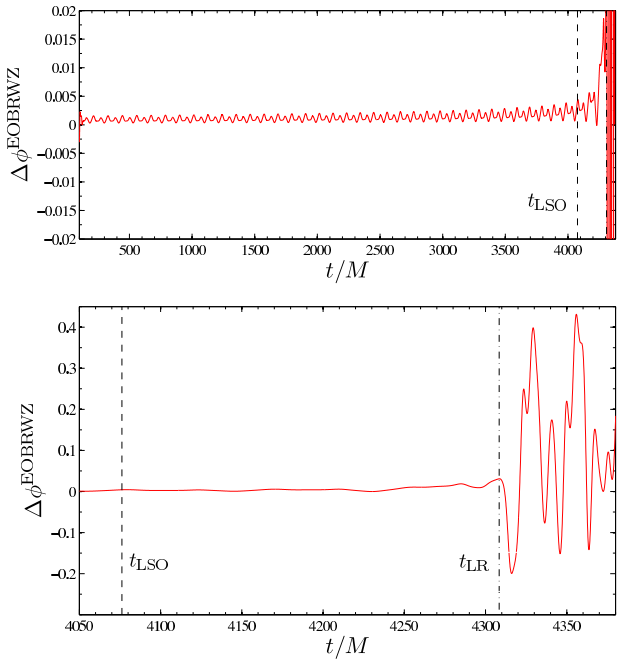

FIG. 7. Time-evolution of the phase difference $\Delta\phi^{\rm EOBRWZ} = \phi^{\rm EOB} - \phi^{\rm RWZ}$ between the EOB and RWZ waveforms of Fig. 6. The top panel displays the behavior of this function from the very beginning (corresponding to initial separation $r = 7M$); the bottom panel focuses on the late-time behavior.

form. Second, we do not further calibrate the $\nu = 0$ EOB-resummed flux (and thus the radiation reaction $\mathcal{F}_\varphi$) to circularized exact data [58]. We believe that an additional tuning of higher PN contributions to the flux, though necessary for dynamical accuracy, would have only a marginal influence on our results.

We finally remark that our setup and the accuracy of our data permitted us to assess the quality of the approximation to the $\delta_{\ell m}$'s residual phases entering the EOB waveform. Note that we have used the $\delta_{\ell m}$'s in their standard Taylor-expanded form [8, 46] and we have not attempted to further resum them using nonpolynomial expressions. This might certainly be interesting to explore to further reduce the (small) phase gap we have at the beginning of the evolution.

Transition from inspiral to plunge, merger and ringdown. For the first time we have explored the impact of NQC corrections to the complete multipolar waveform, including higher multipoles with $2 \leq \ell \leq 4$. The addition of NQC corrections is important to improve the EOB/RWZ modulus and phase agreement towards merger. We have proposed a simple procedure to determine NQC corrections on both phase and amplitude for each multipole; four parameters are required, two for the amplitude and two for the phase. They are determined by imposing compatibility between EOB and RWZ waveform amplitude, frequency, and their first derivatives at the light-ring, *i.e.* the maximum of the orbital frequency. The procedure is robust and applies directly to all multipoles (including those with $\ell > 4$, that we have not explicitly discussed in the text). The complete EOB gravitational waveform (summed up to $\ell = 4$) shows a remarkably good phasing and amplitude agreement with the numerical one up to merger (± 0.015 rad). After the light-ring crossing we have a total phase difference of about 0.25 due to the approximate treatment of the ringdown (via matching to QNMs), although it mainly oscillates around zero. The maximum relative amplitude difference is about 2.5% just before the light-ring. We emphasize that the exquisite phase agreement that we find at merger crucially relies on the calibration of NQC corrections to the phase.

The procedure discussed here to determine the NQC corrections can be directly applied to EOB/NR comparisons for comparable mass ratios generalizing current techniques. However, when $\nu \neq 0$, the procedure is more complicated due to the dependence of the EOB dynamics, notably of the Hamiltonian, on other flexibility parameters that also require to be determined (or constrained) by NR data. In particular, one of the most evident physical effects entailed by these corrections on the dynamics is to displace the location of the "EOB-light-ring" (*i.e.* the maximum of Ω), and thus the location of the matching time t_m. In our $\nu = 0$ setting we can identify on the waveform unambiguously the time $t_{\rm LR}$ that corresponds to the crossing of the light-ring, because of the very good ($\sim 10^{-4}$ rad) phase alignment of the waveforms at early times, and because the underlying dynamics is the same. This allows us to measure the useful RWZ information at the correct location. As we emphasized in the text t_m *does not* coincide with the time when A_{22} peakes, but it occurs $2.56M$ earlier. On the other hand, when dealing with NR data, the exact dynamics is not evidently available and one can rely only on waveform information. The peak of the "exact" orbital frequency, if it existed, should occur slightly after the peak of the A_{22} metric waveform amplitude. As a consequence, to apply the same discussed here to fix the NQC parameters, and to keep the maximum of Ω as matching point, one should measure the four numbers per multipoles slightly (say by $\sim 1M$) after the peak of A_{22}. This method is different from current methods in EOB/NR comparisons, *i.e.* fix the NQC amplitude corrections imposing that the EOB and NR A_{22} peaks *coincide* at the maximum of the EOB orbital frequency. Even if this procedure is not a priori incorrect, we stress that if we were following this prescription in our setup we would have obtained a significantly larger phase difference ($\sim \quad -0.2$ rad), accumulated (starting from the 10^{-2} level) in the last $50M$ before merger. This suggests that a more detailed analysis of the impact of NQC corrections to EOB waveforms in the comparable mass case might be needed in the future.

As a last remark, we emphasize that extraction of numerical waveforms at null infinity convinced us to avoid any further (arbitrary) phase and time shift, providing clean information about the accuracy of the analytical

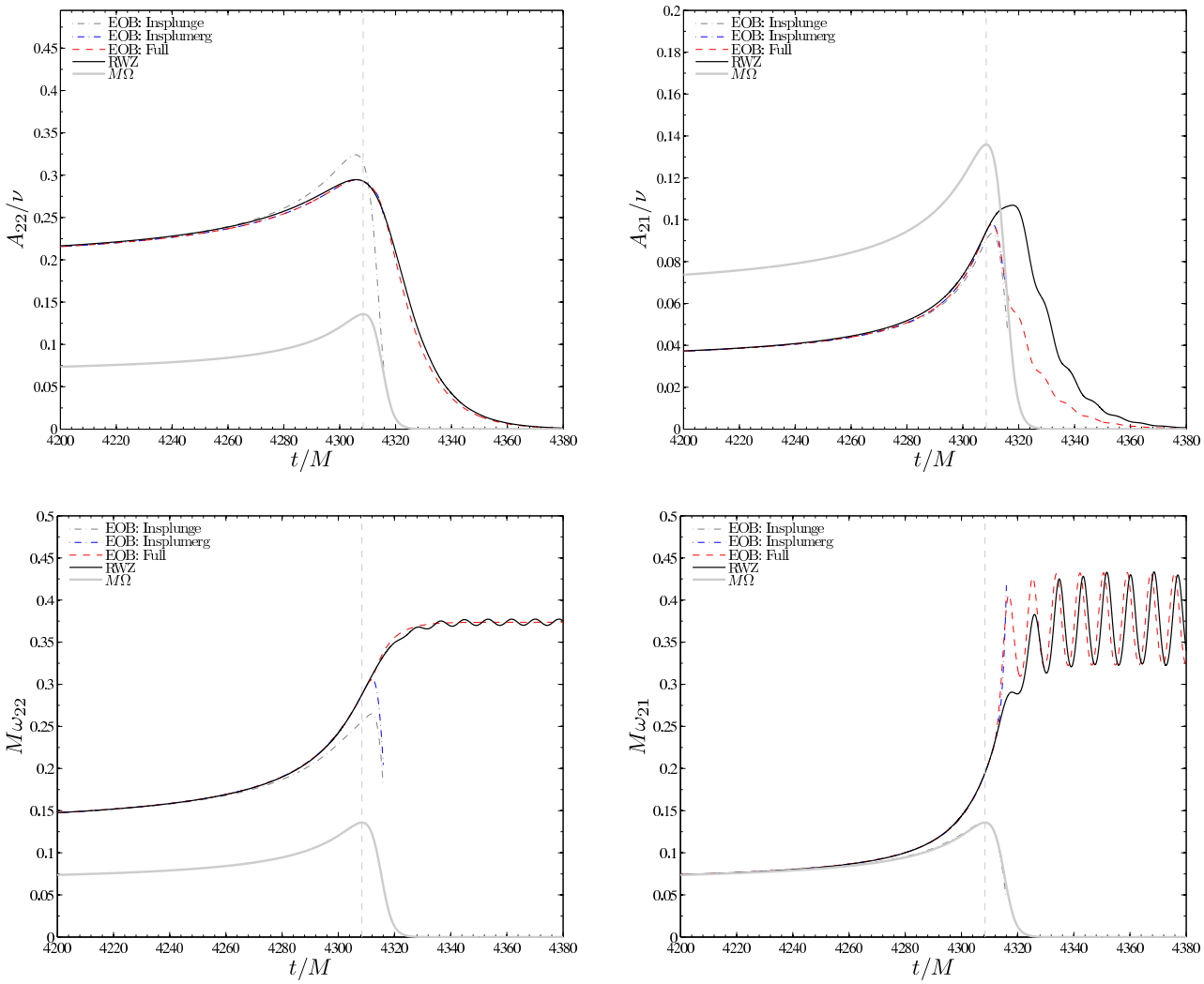

FIG. 8. Improvement of the EOB $\ell = 2$ ringdown waveform when matching the QNMs at $t_{\rm match} = t_{\rm LR} + 3M$. As in Fig. 3, The (light) dashed lines refer to the bare insplunge waveform, without the addition of NQC corrections (dash-dotted, blue online) nor of QNM ringdown (dashed, red online). The vertical dashed-line locates the maximum of $M\Omega$.

modeling of the GW phase in the EOB waveform. On the contrary, we have shown that waveforms extracted at the finite radius $r_* = 1000M$ yield initial phase differences (with the EOB ones) during the inspiral that are $\sim 3\times10^{-2}$ rad for the (2,2) multipole and about twice as much, $\sim 5.5\times10^{-2}$ rad, for the (2,1) multipole (and even larger for the subdominant multipoles [48]). This fact strongly indicates, once more, that in any EOB/NR comparison it is *necessary* to work either with NR waveforms extrapolated to infinite extraction radius or evolved up to null infinity [59, 60].

ACKNOWLEDGMENTS

We thank Thibault Damour for useful inputs. SB is supported by DFG Grant SFB/Transregio 7 "Gravitational Wave Astronomy". SB thanks IHES for hospitality and support during the development of this work. Computations were performed on the `Merlin` cluster at IHES. AZ is supported by the Agence Nationale de la Recherche (ANR) grant 06-2-134423 in Paris, by the NSF grant PHY-0601459 and by a Sherman Fairchild Foundation grant to Caltech in Pasadena.

Appendix A: QNM matching at $t_{\rm match} > t_{\rm LR}$

In this Appendix we briefly explore how the quality of the post-merger waveform depends on shifting the matching to QNMs at $t_{\rm match} > t_{\Omega_{\rm max}} = t_{\rm LR}$, maintaining the determination of the NQC parameters at $t = t_{\rm LR}$. While the results of Sec. IV and V are already satisfactory, we experimentally observe that displacing the matching to QNMs by $\Delta t = t_{\rm match} - t_{\rm LR} \sim 3M$ produces a further improvement in the final waveform. This approach is

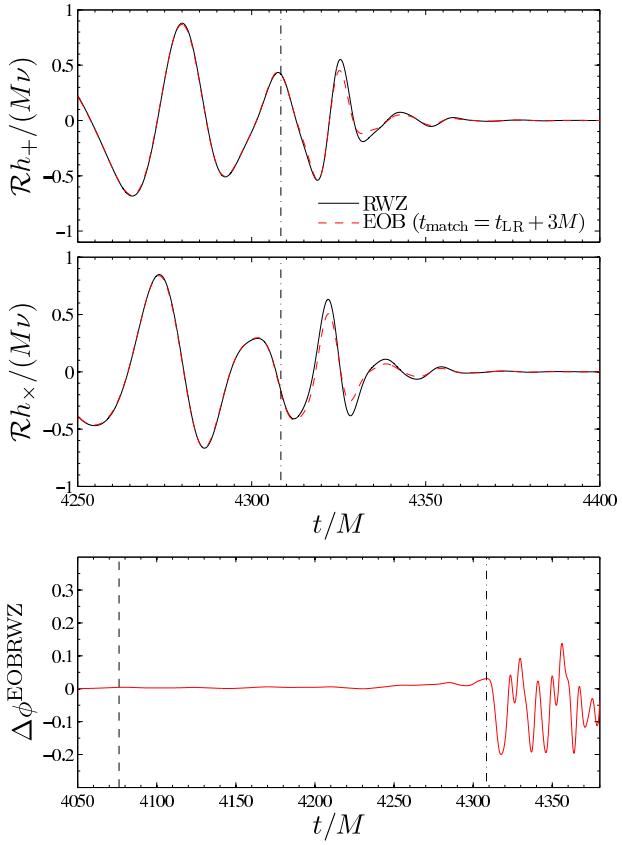

FIG. 9. Improvement of the EOB ringdown waveform when matching the QNMs at $t_{\rm match}=t_{\rm LR}+3M$. Top panels: h_+ and $h_\times$ GW polarizations. Bottom panel: phase difference. Contrast it with Figs. 6 and 7. The dashed-dotted vertical lines indicates the light-ring crossing.

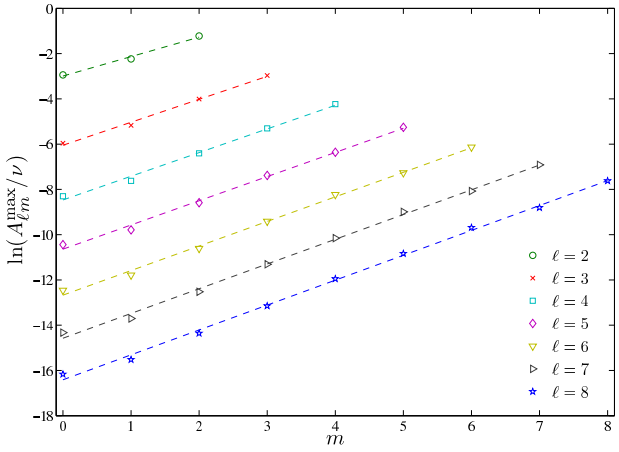

FIG. 10. Maxima of the modulus of the RWZ master function for different multipoles. The dashed lines are obtained by fitting the data with Eq. (B1).

also suggested by a careful inspection of Fig. 3 in the region around $t_{\rm LR}$: it is clear that (for both multipoles) the EOB insplumerg frequency and amplitude want to remain close to the numerical one even *after* $t=t_{\rm LR}$, so that we do not seem to be strictly obliged to just match the QNMs at $t_m=t_{\rm LR}$. The result of matching QNMs at a shifted time is shown in Fig. 8 for $\ell=2$ (compare it with Fig. 3). The improvement in the closeness between frequencies and amplitude during the ringdown is striking especially for the $m=2$ mode. An analogous result is obtained for the other multipoles, the more important improvement affecting the $m=\ell$ modes. Concerning the $\ell=2$, $m=1$ mode (and similarly for other odd-parity multipoles with $\ell>2$) one succeeds in having a more accurate representation of the oscillation in the frequency due to the interference between positive and negative frequency modes. On the contrary, the amplitude differences in the ringdown are still present.

The influence that the match to QNMs at $t_{\rm match}>t_{\rm LR}$ has on the total waveform (summed up to $\ell=4$) can be appreciated in Fig. 9 for the two GW polarizations $(h_+,h_\times)$ (top panels, contrast them with Fig. 6) and for the total phase difference (bottom panel, contrast it with Fig. 7). Notably, in the latter plot the amplitude of the oscillation in the phase difference is more than a factor 2 smaller than the standard case. The result is mainly due to the relatively inaccurate representation of the ringdown of the (2,1) mode.

Appendix B: Multipolar hierarchy at merger

In this Appendix we study how the waveform amplitude peaks $A^{\rm max}_{\ell m}=\max(A_{\ell m})$ depend on the multipolar order (ℓ,m). The numerical values of $A^{\rm max}_{\ell m}$ present some regularities that it is worth to discuss in some detail. In Fig. 10 we show $A^{\rm max}_{\ell m}/\nu$ for all multipoles up to $\ell=8$. The corresponding numerical values are listed in Table VI for completeness. The multipolar structure is such that the peak of the waveform amplitude is about ten times smaller when the azimuthal number ℓ decreases by one (for a fixed m), while, for a given ℓ, it increases with m. As an example, the maximum amplitude of the multipole (4,3) is larger than the (3,0) one.

A fit of the $A^{\rm max}_{\ell m}$ data of Table VI with the functional form

$$\ln\left(A^{\rm max}_{\ell m}\right)=c_1(\ell)m+c_2(\ell)\ell \qquad \text{(B1)}$$

shows that the behavior of the $A^{\rm max}_{\ell m}$ is approximately exponential in m for each ℓ; for each value of m $A^{\rm max}_{\ell m}$, scales approximately as $\mathrm{e}^{2\ell}$ when $\ell>2$, *i.e.* we have $A^{\rm max}_{\ell m}\approx \mathrm{e}^{m-2\ell}$. The precise numerical values of $c_1(\ell)$ and $c_2(\ell)$ are listed in Table V, together with the coefficient of determination R^2 that measures the quality of the fit [4].

[4] The coefficient of determination is defined as

$$R^2\equiv 1-\frac{\sum_i(y_i-\hat{y}_i)^2}{\sum_i(y_i-\bar{y})^2}$$

TABLE V. Fit of the maxima of the modulus of the RWZ for different ℓ-multipoles as function of m. The fit assumes the functional form Eq. (B1). The 90% confidence interval of the estimate coefficients is reported as well as the coefficient of determination, R^2.

ℓ	$c_1(\ell)$	90% Conf.	$c_2(\ell)$	90% Conf.	R^2
2	0.86	[0.87 0.85]	-1.497	[-1.491 -1.502]	0.989
3	1.02	[1.02 1.00]	-2.016	[-2.013 -2.019]	0.995
4	1.05	[1.06 1.04]	-2.116	[-2.114 -2.119]	0.993
5	1.07	[1.08 1.06]	-2.128	[-2.126 -2.130]	0.995
6	1.09	[1.10 1.08]	-2.112	[-2.111 -2.113]	0.997
7	1.09	[1.10 1.08]	-2.082	[-2.081 -2.083]	0.997
8	1.10	[1.11 1.09]	-2.051	[-2.050 -2.052]	0.998

We finally note that the value for $A_{22}^{\rm max}/\nu$ that we obtain here is not dramatically different from the values obtained when the masses m_1 and m_2 are comparable. For example, the value $(A_{22}^{\rm max}/\nu)_{\nu=0} = 0.295$ is about a 10% smaller than the corresponding numerical value computed the equal-mass case, $q = m_2/m_1 = 1$, $(A_{22}^{\rm max})/\nu)_{q=1} \sim 0.321$ and only about a 6% smaller when $q = 4$, $(A_{22}^{\rm max}/\nu)_{q=4} \sim 0.31$. As already pointed out in [6], one can fit the values of $A_{22}^{\rm max}/\nu$ obtained from a few (accurate) numerical-relativity simulations as a function of $\eta = (1-4\nu)$, where $\nu = m_1 m_2/(m_1+m_2)^2$ is the symmetric mass ratio and reduces to $\nu = \mu/M$ when $m_1 \ll m_2$. Assuming a linear behavior in η, as it was done in [6], one obtains $A_{22}^{\rm max} \simeq 0.321\nu[1 - 0.0899(1-4\nu)]$. However, it turns out that a better representation of the data is given by a *quadratic* behavior in $(1-4\nu)$ of the form $A_{22}^{\rm max} \simeq 0.321\nu[1 - 0.0162(1-4\nu) + 0.0792(1-4\nu)^2]$. In the future it will be interesting to check the numerical accuracy of this relation versus other NR data, as well as to generalize it to the other multipoles.

where y_i is the observed data set, $\bar{y}$ its average and $\hat{y}_i$ the predicted data set. $R^2 \in [0,1]$ is the square of the correlation coefficient [61] and it gives the percent of the variance in $\hat{y}_i$ predictable from y_i

TABLE VI. Information about the maxima of the modulus of the RWZ multipoles. For each multipole we report the time shift between the time location of the maximum $t^{\ell m}_{\rm max}$ and the light-ring crossing time $t_{\rm LR}$, the maximum of the modulus of the RWZ waveform, its derivative at $t_{\rm LR}$, the frequency and its derivative at $t^{\ell m}_{\rm max}$.

ℓ	m	$(t^{\ell m}_{\rm max} - t_{\rm LR})$	$A^{\rm max}_{\ell m}$	$\dot{A^{\rm max}_{\ell m}}(t^{\ell m}_{\rm max})$	$M\omega_{\ell m}(t^{\ell m}_{\rm max})$	$M\dot{\omega}_{\ell m}(t^{\ell m}_{\rm max})$
2	0	1.106×10^{1}	0.527×10^{-1}	-0.220×10^{-4}	0.790×10^{-21}	0.149×10^{-18}
2	1	9.400×10^{0}	0.107×10^{-0}	0.258×10^{-5}	0.291×10^{-0}	0.591×10^{-3}
2	2	-2.560×10^{0}	0.295×10^{-0}	-0.260×10^{-5}	0.272×10^{-0}	0.587×10^{-2}
3	0	1.036×10^{1}	0.258×10^{-2}	0.208×10^{-5}	0.313×10^{-19}	-0.739×10^{-17}
3	1	1.054×10^{1}	0.569×10^{-2}	0.767×10^{-6}	0.411×10^{-0}	0.679×10^{-2}
3	2	6.840×10^{0}	0.182×10^{-1}	-0.108×10^{-5}	0.452×10^{-0}	0.159×10^{-1}
3	3	1.000×10^{0}	0.515×10^{-1}	-0.519×10^{-6}	0.453×10^{-0}	0.109×10^{-1}
4	0	1.508×10^{1}	0.248×10^{-3}	0.321×10^{-6}	-0.523×10^{-18}	0.190×10^{-15}
4	1	1.072×10^{1}	0.488×10^{-3}	0.572×10^{-7}	0.552×10^{-0}	0.371×10^{-1}
4	2	9.520×10^{0}	0.165×10^{-2}	0.158×10^{-7}	0.626×10^{-0}	0.196×10^{-1}
4	3	7.200×10^{0}	0.497×10^{-2}	0.686×10^{-7}	0.637×10^{-0}	0.189×10^{-1}
4	4	2.820×10^{0}	0.145×10^{-1}	-0.225×10^{-6}	0.634×10^{-0}	0.152×10^{-1}
5	0	1.424×10^{1}	0.293×10^{-4}	-0.178×10^{-6}	-0.208×10^{-16}	-0.244×10^{-14}
5	1	1.422×10^{1}	0.562×10^{-4}	0.547×10^{-7}	0.745×10^{-0}	-0.110×10^{-1}
5	2	1.122×10^{1}	0.186×10^{-3}	0.390×10^{-7}	0.807×10^{-0}	0.312×10^{-1}
5	3	9.140×10^{0}	0.622×10^{-3}	-0.501×10^{-7}	0.801×10^{-0}	0.263×10^{-1}
5	4	7.620×10^{0}	0.173×10^{-2}	-0.302×10^{-7}	0.822×10^{-0}	0.222×10^{-1}
5	5	4.120×10^{0}	0.521×10^{-2}	-0.268×10^{-6}	0.817×10^{-0}	0.189×10^{-1}
6	0	1.664×10^{1}	0.388×10^{-5}	-0.283×10^{-7}	0.188×10^{-15}	0.299×10^{-13}
6	1	1.376×10^{1}	0.758×10^{-5}	-0.595×10^{-8}	0.880×10^{-0}	0.332×10^{-1}
6	2	1.332×10^{1}	0.246×10^{-4}	0.461×10^{-8}	1.021×10^{0}	0.102×10^{-1}
6	3	1.128×10^{1}	0.818×10^{-4}	-0.199×10^{-8}	1.001×10^{0}	0.297×10^{-1}
6	4	9.240×10^{0}	0.266×10^{-3}	0.254×10^{-7}	0.985×10^{-0}	0.288×10^{-1}
6	5	8.080×10^{0}	0.697×10^{-3}	-0.247×10^{-7}	1.008×10^{0}	0.249×10^{-1}
6	6	5.140×10^{0}	0.216×10^{-2}	-0.550×10^{-7}	1.002×10^{0}	0.222×10^{-1}
7	0	1.588×10^{1}	0.598×10^{-6}	-0.332×10^{-8}	-0.929×10^{-15}	-0.256×10^{-12}
7	1	1.588×10^{1}	0.112×10^{-5}	-0.212×10^{-8}	1.063×10^{0}	-0.878×10^{-2}
7	2	1.364×10^{1}	0.365×10^{-5}	-0.350×10^{-9}	1.186×10^{0}	0.416×10^{-1}
7	3	1.252×10^{1}	0.123×10^{-4}	-0.128×10^{-8}	1.189×10^{0}	0.330×10^{-1}
7	4	1.128×10^{1}	0.390×10^{-4}	-0.131×10^{-8}	1.186×10^{0}	0.319×10^{-1}
7	5	9.460×10^{0}	0.124×10^{-3}	0.505×10^{-8}	1.171×10^{0}	0.311×10^{-1}
7	6	8.540×10^{0}	0.311×10^{-3}	-0.238×10^{-7}	1.195×10^{0}	0.273×10^{-1}
7	7	6.000×10^{0}	0.993×10^{-3}	-0.692×10^{-7}	1.188×10^{0}	0.250×10^{-1}
8	0	1.746×10^{1}	0.951×10^{-7}	0.700×10^{-9}	-0.774×10^{-14}	0.223×10^{-11}
8	1	1.534×10^{1}	0.181×10^{-6}	-0.336×10^{-9}	1.199×10^{0}	0.460×10^{-1}
8	2	1.524×10^{1}	0.579×10^{-6}	0.141×10^{-9}	1.400×10^{0}	0.728×10^{-2}
8	3	1.366×10^{1}	0.195×10^{-5}	0.205×10^{-9}	1.386×10^{0}	0.364×10^{-1}
8	4	1.242×10^{1}	0.646×10^{-5}	-0.699×10^{-9}	1.372×10^{0}	0.354×10^{-1}
8	5	1.136×10^{1}	0.197×10^{-4}	0.547×10^{-10}	1.373×10^{0}	0.338×10^{-1}
8	6	9.720×10^{0}	0.621×10^{-4}	0.396×10^{-8}	1.359×10^{0}	0.332×10^{-1}
8	7	8.960×10^{0}	0.150×10^{-3}	0.153×10^{-7}	1.383×10^{0}	0.294×10^{-1}
8	8	6.720×10^{0}	0.490×10^{-3}	0.238×10^{-7}	1.375×10^{0}	0.276×10^{-1}

[1] A. Buonanno, Y. Pan, J. G. Baker, J. Centrella, B. J. Kelly, S. T. McWilliams and J. R. van Meter, Phys. Rev. D **76**, 104049 (2007)

[2] T. Damour and A. Nagar, Phys. Rev. D **77**, 024043 (2008)

[3] T. Damour, A. Nagar, E. N. Dorband, D. Pollney and L. Rezzolla, Phys. Rev. D **77**, 084017 (2008)

[4] T. Damour, A. Nagar, M. Hannam, S. Husa and B. Bruegmann, Phys. Rev. D **78**, 044039 (2008)

[5] M. Boyle, A. Buonanno, L. E. Kidder, A. H. Mroue, Y. Pan, H. P. Pfeiffer and M. A. Scheel, Phys. Rev. D **78**, 104020 (2008)

[6] T. Damour and A. Nagar, Phys. Rev. D **79**, 081503 (2009) [arXiv:0902.0136 [gr-qc]].

[7] A. Buonanno, Y. Pan, H. P. Pfeiffer, M. A. Scheel, L. T. Buchman and L. E. Kidder, Phys. Rev. D **79**, 124028 (2009)

[8] T. Damour, B. R. Iyer and A. Nagar, Phys. Rev. D **79**, 064004 (2009)

[9] T. Damour, Phys. Rev. D **81**, 024017 (2010) [arXiv:0910.5533 [gr-qc]].

[10] Y. Pan, A. Buonanno, L. T. Buchman, T. Chu, L. E. Kidder, H. P. Pfeiffer and M. A. Scheel, Phys. Rev. D **81**, 084041 (2010)

[11] T. Damour and A. Nagar, arXiv:0906.1769 [gr-qc].

[12] F. Pretorius, Phys. Rev. Lett. **95**, 121101 (2005)

[13] J. A. Gonzalez, U. Sperhake and B. Bruegmann, Phys. Rev. D **79**, 124006 (2009)

[14] D. Pollney, C. Reisswig, E. Schnetter, N. Dorband and P. Diener, arXiv:0910.3803 [gr-qc].

[15] C. O. Lousto, H. Nakano, Y. Zlochower and M. Campanelli, Phys. Rev. Lett. **104**, 211101 (2010)

[16] C. O. Lousto and Y. Zlochower, arXiv:1009.0292 [gr-qc].

[17] J. R. Gair, L. Barack, T. Creighton, C. Cutler, S. L. Larson, E. S. Phinney and M. Vallisneri, Class. Quant. Grav. **21**, S1595 (2004)

[18] A. Buonanno and T. Damour, Phys. Rev. D **59**, 084006 (1999)

[19] A. Buonanno and T. Damour, Phys. Rev. D **62**, 064015 (2000)

[20] T. Damour, P. Jaranowski and G. Schaefer, Phys. Rev. D **62**, 084011 (2000)

[21] T. Damour, Phys. Rev. D **64**, 124013 (2001)

[22] A. Buonanno, Y. Chen and T. Damour, Phys. Rev. D **74**, 104005 (2006)

[23] T. Damour, B. R. Iyer, P. Jaranowski and B. S. Sathyaprakash, Phys. Rev. D **67**, 064028 (2003)

[24] T. Regge and J. A. Wheeler, Phys. Rev. **108**, 1063 (1957).

[25] F. J. Zerilli, Phys. Rev. Lett. **24**, 737 (1970).

[26] K. Martel and E. Poisson, Phys. Rev. D **71**, 104003 (2005)

[27] A. Nagar and L. Rezzolla, Class. Quant. Grav. **22**, R167 (2005) [Erratum-ibid. **23**, 4297 (2006)]

[28] T. Damour, B. R. Iyer and B. S. Sathyaprakash, Phys. Rev. D **57**, 885 (1998)

[29] T. Damour and A. Nagar, Phys. Rev. D **76**, 064028 (2007)

[30] N. Yunes, A. Buonanno, S. A. Hughes, M. Coleman Miller and Y. Pan, Phys. Rev. Lett. **104**, 091102 (2010)

[31] N. Yunes, A. Buonanno, S. A. Hughes, Y. Pan, E. Barausse, M. C. Miller and W. Throwe, arXiv:1009.6013 [gr-qc].

[32] L. Barack and N. Sago, Phys. Rev. Lett. **102**, 191101 (2009)

[33] L. Barack and N. Sago, Phys. Rev. D **81**, 084021 (2010)

[34] L. Barack, T. Damour and N. Sago, Phys. Rev. D **82**, 084036 (2010)

[35] E. Berti, V. Cardoso, T. Hinderer *et al.*, Phys. Rev. **D81**, 104048 (2010).

[36] M. Davis, R. Ruffini and J. Tiomno, Phys. Rev. D **5**, 2932 (1972).

[37] A. Nagar, J. A. Font, O. Zanotti and R. De Pietri, Phys. Rev. D **72**, 024007 (2005)

[38] A. Nagar, G. Diaz, J. A. Pons and J. A. Font, Phys. Rev. D **69**, 124028 (2004)

[39] P. Canizares and C. F. Sopuerta, arXiv:1009.6073 [gr-qc].

[40] K. Martel and E. Poisson, Phys. Rev. D **66**, 084001 (2002)

[41] K. Martel, Phys. Rev. D **69**, 044025 (2004)

[42] C. F. Sopuerta and P. Laguna, Phys. Rev. D **73**, 044028 (2006) [arXiv:gr-qc/0512028].

[43] A. Nagar, T. Damour and A. Tartaglia, Class. Quant. Grav. **24**, S109 (2007)

[44] P. A. Sundararajan, G. Khanna and S. A. Hughes, Phys. Rev. D **81**, 104009 (2010)

[45] S. Bernuzzi and A. Nagar, Phys. Rev. D **81**, 084056 (2010)

[46] R. Fujita and B. R. Iyer, Phys. Rev. D **82**, 044051 (2010)

[47] J. A. Gonzalez, U. Sperhake, B. Bruegmann, M. Hannam and S. Husa, Phys. Rev. Lett. **98**, 091101 (2007) [arXiv:gr-qc/0610154].

[48] S. Bernuzzi, A. Nagar and A. Zenginoglu, in preparation (2010).

[49] A. Zenginoglu, J. Comput. Phys. **230**, 2286-2302 (2011) [arXiv:1008.3809 [math.NA]].

[50] A. Zenginoglu, Class. Quant. Grav. **27**, 045015 (2010) [arXiv:0911.2450 [gr-qc]].

[51] A. Zenginoglu, Class. Quant. Grav. **25**, 145002 (2008)

[52] O. Sarbach, M. Tiglio, Phys. Rev. **D64**, 084016 (2001). [gr-qc/0104061].

[53] L. Blanchet, S. L. Detweiler, A. Le Tiec and B. F. Whiting, Phys. Rev. D **81**, 064004 (2010)

[54] L. E. Kidder, Phys. Rev. D **77**, 044016 (2008)

[55] T. Damour and A. Gopakumar, Phys. Rev. D **73**, 124006 (2006)

[56] A. Ori and K. S. Thorne, Phys. Rev. D **62**, 124022 (2000)

[57] E. Berti, V. Cardoso, C. M. Will, Phys. Rev. **D73**, 064030 (2006).

[58] R. Fujita, W. Hikida and H. Tagoshi, Prog. Theor. Phys. **121**, 843 (2009)

[59] C. Reisswig, N. T. Bishop, D. Pollney and B. Szilagyi, Class. Quant. Grav. **27**, 075014 (2010)

[60] C. Reisswig, N. T. Bishop, D. Pollney and B. Szilagyi, Phys. Rev. Lett. **103**, 221101 (2009)

[61] J. R. Taylor. "An Introduction to Error Analysis." University Science Books, Oxford, (1982).